

PHD THESIS

UNIVERSITÀ DEGLI STUDI DI NAPOLI “FEDERICO II”

DIPARTIMENTO DI INGEGNERIA BIOMEDICA ELETTRONICA
E DELLE TELECOMUNICAZIONI

DOTTORATO DI RICERCA IN
INGEGNERIA ELETTRONICA E DELLE TELECOMUNICAZIONI

INNOVATIVE FRACTAL-BASED
MODELS
FOR RADAR ALTIMETER DATA

GABRIELLA BERNARDI

Il Coordinatore del Corso di Dottorato

Ch.mo Prof. Niccolò RINALDI

Il Tutore

Ch.mo Prof. Daniele RICCIO

A. A. 2010-2011

Acknowledgments

It is a pleasure to thank the many people who made this Thesis possible.

I want to first express my deep gratitude to my Ph.D. supervisor, prof. Daniele Riccio. Throughout my Ph.D. course, he provided good teaching, encouragement and lots of inspiring ideas. I learned from him to never give up.

I thank the professor Giorgio Franceschetti, for giving me the chance to collaborate with the JPL (NASA). Obviously, special thanks go to the members of the Cassini Radar Science Team for the helpful discussions.

I wish also to thank Dr. Michele D'Urso, my head in SELEX-SI, for giving me the possibility to complete my Ph.D., accepting to share my working time with the University. I want to also thank Dr. Giancarlo Prisco. Even if I worked with him for a short time, he was able to transmit to me the passion for his work, and, more in general, the love for knowledge.

I would also take this opportunity to thank the people who have taught me something important and who have left a sign into my professional life. At first my parents, who have taught me, by example, the most important of the lessons in life, the sense of duty. I have learned from them that working hardly and honestly gives you the serenity and the strength to face every kind of problem, and, above all, allows you to not confuse the right and the for. Another crucial figure in my life is Mrs. Carmen Raucci, my piano teacher. She always taught me the importance of being self-critical, and, in particular, she always pushed me towards a relentless research of personal improvement.

I wish finally thank the many people who have supported me during this journey: my brothers, my boyfriend, my friends, the old and the new ones. I cannot list them because they are too many and this page would not be enough, but every one of them internally knows how important he/she has been for me.

Contents

Acknowledgments	iii
List of Figures	vii
List of Tables	xi
Acronyms	xiii
Introduction	xv
1 Fundamentals	1
1.1 Radar Satellite Altimetry Basics	1
1.2 Standard Processing Techniques	5
1.2.1 Ideal flat surface investigation	6
1.2.2 Natural land surface investigation	8
1.3 Radar Satellite Altimetry Missions Overview	9
2 Developments in radar altimetry	17
2.1 The reference model of Brown	17
2.2 Recent Developments	19
3 Natural surfaces and fractals	23
3.1 Fractal description of natural surfaces	24
3.2 Fractional brownian motion process	25
3.3 Weierstrass-Mandelbrot function	27
3.4 Connection between WM and fBm surfaces	29
4 Fractal Based Model of Altimeter Data	31
4.1 The rationale of the proposed approach	31

4.2	Waveform Modeling	33
4.3	Surface Modeling	34
4.4	Electromagnetic Scattering	38
5	Numerical Results	41
5.1	Planar Surface	44
5.2	Tilted Surface	45
5.3	Sinusoidal Surface	46
5.4	Layered Surface	46
5.5	Fractal Surface	47
6	Experimental validation	59
6.1	Cassini Mission Radar Altimeter	59
6.1.1	The Cassini Radar	60
6.1.2	Cassini PAD System Overview	61
6.2	The proposed model in the Cassini framework	65
6.2.1	Estimating fractal parameters	66
6.2.2	Validation results	68
	Conclusion	73
	Bibliography	75

List of Figures

1.1	Geometry out of scale	4
1.2	On the left, a 3D picture, out of scale, of the scenario with a visible surface topography; on the right a 2D section of the same scenario.	5
1.3	An example of waveform received on ocean surfaces, from Poseidon mission.	7
1.4	A typical waveform received on ocean surfaces.	7
1.5	Seasat spacecraft, courtesy of NASA.	10
1.6	Earth coverage map, Seasat mission.	10
4.1	Section (out of scale) of the geometry of the system relevant to the problem: the reference surfaces are depicted. In (a) the reference surface is the plane $z = 0$, tangent to the planet, whose profile is described by $z(x, y)$, without taking into account the planet curvature whose shape is only indicated, but plays no role in the profile definition; in (b) the reference surface is the planet ideal shape, the sphere S_T , and the planet profile is described by $[z(x, y) - \Delta h(x, y)]$, thus taking into account the planet curvature.	36
4.2	Global system.	38
4.3	Geometry of the scattering problem.	40
5.1	Logical scheme of the simulation procedure.	42

-
- 5.2 Simulated echo power, normalized to its peak value, from a surface: 5.2(a) flat at footprint scale, smooth at wavelength scale, 1 pulse; 5.2(b) flat at footprint scale, rough at wavelength scale, 1 pulse; 5.2(c) flat at footprint scale, rough at wavelength scale, average over 15 transmitted pulses. The echo power is represented by diamonds and its linear interpolation is represented by the solid line. The dotted line shows the impulse response of the system. 49
- 5.3 Simulated echo power, normalized to its peak value, from a surface tilted at footprint scale, rough at wavelength scale: 5.3(a) 1 pulse; 5.3(b) average over 15 transmitted pulses; 5.3(c) average over an infinite number of transmitted pulses. The echo power is represented by diamonds and its linear interpolation is represented by the solid line. The dotted line shows the impulse response of the system. 50
- 5.4 Simulated echo power, normalized to its peak value, from a surface sinusoidal at footprint scale (amplitude = 100 m, wavelength = 3000 m) rough at wavelength scale: 5.4(a) 1 pulse; 5.4(b) average over 15 transmitted pulses; 5.4(c) average over an infinite number of transmitted pulses. The echo power is represented by diamonds and its linear interpolation is represented by the solid line. The dotted line shows the impulse response of the system. 51
- 5.5 5.5(a) Sketch of the layered geometry. The first layer is rough at wavelength scale, the second one is smooth. $\epsilon_r = 3, \sigma = 10^{-7} S/m$. In the subsequent subfigures the received power echo, normalized to its peak value. The layer thickness is $d = 100m$. 5.5(b) 1 pulse; 5.5(c) average over 15 transmitted pulses; 5.5(d) average over an infinite number of transmitted pulses. The echo power is represented by diamonds and its linear interpolation is represented by the solid line. The dotted line shows the impulse response of the system. 52

5.6	5.6(a) Sketch of the layered geometry. The first layer is rough at wavelength scale, the second one is smooth. $\epsilon_r = 3, \sigma = 10^{-7} S/m$. In the subsequent subfigures the received power echo, normalized to its peak value. The layer thickness is $d = 50m$. 5.6(b) 1 pulse; 5.6(c) average over 15 transmitted pulses; 5.6(d) average over an infinite number of transmitted pulses. The echo power is represented by diamonds and its linear interpolation is represented by the solid line. The dotted line shows the impulse response of the system.	53
5.7	Received power echo, normalized to its peak value, from a fractal surface 5.7(a) at both footprint and wavelength scale ($H = 0.6, B = 500m$); 5.7(b) 1 pulse; 5.7(c) average over 15 transmitted pulses; 5.7(d) average over an infinite number of transmitted pulses. The echo power is represented by diamonds and its linear interpolation is represented by the solid line. The dotted line shows the impulse response of the system.	54
5.8	Received power echo, normalized to its peak value, from a fractal surface 5.8(a) at both footprint and wavelength scale ($H = 0.6, B = 250m$); 5.8(b) 1 pulse; 5.8(c) average over 15 transmitted pulses; 5.8(d) average over an infinite number of transmitted pulses. The echo power is represented by diamonds and its linear interpolation is represented by the solid line. The dotted line shows the impulse response of the system.	55
5.9	Received power echo, normalized to its peak value, from a fractal surface 5.9(a) at both footprint and wavelength scale ($H=0.6, B=500m$, same as Fig. 5.7) with off-nadir pointing of 1.8 deg (like slope in Fig. 5.3; 5.9(b) 1 pulse; 5.9(c) average over 15 transmitted pulses; 5.9(d) average over an infinite number of transmitted pulses. The echo power is represented by diamonds and its linear interpolation is represented by the solid line. The dotted line shows the impulse response of the system.	56
5.10	5.10(a) WM surface profile with $H=0.6, B=500m$; 5.10(b) Corresponding echogram by using the simulated return pulses. . .	57
5.11	5.11(a) WM surface profile with $H=0.6, B=250m$; 5.11(b) Corresponding echogram by using the simulated return pulses. . .	58
6.1	Sketch of the logical steps followed in the model validation on the Cassini altimeter data.	66

6.2	Flyby T19 detected profile with the relative echogram and three different received pulses (averaged on the relative bursts).	67
6.3	6.3(a) Received pulse of the burst 634 of the T19 flyby Cassini mission; 6.3(b) simulated pulse. The values of the parameters estimated from the real data are: $H = 0.51, s^2 = 0, 81$; 6.3(c) a cut of the simulated surface; 6.3(d) three-dimensional image of the simulated surface.	69
6.4	6.4(a) Received pulse of the burst 650 of the T19 flyby Cassini mission; 6.4(b) simulated pulse. The values of the parameters estimated from the real data are: $H = 0.6, s^2 = 0, 191$; 6.4(c) a cut of the simulated surface; 6.4(d) three-dimensional image of the simulated surface.	70
6.5	6.5(a) Received pulse of the burst 670 of the T19 flyby Cassini mission; 6.5(b) simulated pulse. The values of the parameters estimated from the real data are: $H = 0.634, s^2 = 0, 143$; 6.5(c) a cut of the simulated surface; 6.5(d) three-dimensional image of the simulated surface.	71

List of Tables

5.1	ALTIMETER SYSTEM PARAMETERS	44
5.2	SURFACE GEOMETRICAL PARAMETERS	44
5.3	FRACTAL SURFACE	45

Acronyms

ASI, Agenzia Spaziale Italiana
ABDR, Altimeter Burst Data Record
BODP, Burst Ordered Data Products
CNES, Centre National d'Etudes Spaciales
ERS, European Remote Sensing satellite
ESA, European Space Agency
fBm, fractional Brownian motion
LBDR, Long Burst Data Record
LIDAR, LIght Detection And Ranging
MT, Map Tool
MLE, Maximum Likelihood Estimation
NASA, National Aeronautics and Space Administration
PAD, Processing of Altimeter Data
PDS, Planetary Data System
PO, Physical Optics
PT, Production Tool
RA, Radar Altimeter
RADAR, RADio Detection and Ranging
RCS, Radar Cross Section
RTG, Radioisotope Thermoelectric Generators
SAR, Synthetic Aperture Radar
SBDR, Short Burst Data Record
SIS, Software Interface Specification
SLT, Science Look Tool
SWH, Significant Wave Height
TD, Threshold Detection
WM, Weierstrass Mandelbrot

Introduction

The altimeter is an active sensor for remote sensing that, as the name itself suggests, estimates the distance from the sensor to an object (typically an extended surface) and, indirectly, the height of that object, above a fixed level. Its frequency range spans from microwaves up to optical frequencies, and is referred to as RADAR (Radio Detection And Ranging) or LIDAR (Light Detection And Ranging) Altimeter, respectively. In this work the Radar Altimeter is considered in its spaceborne configuration: the sensor is located on a satellite platform; the transmitted pulses travel from the satellite to the illuminated surface and back to the satellite, where they are received; time delay is converted in distance from the ground to the satellite (whose position is somehow assumed to be known), thus leading, via appropriate processing, the height profile of the surface. Two classes of methods are mainly used to convert the time delay in the required information: *Threshold Detection* (TD) algorithms and *Maximum Likelihood Estimation* algorithms (MLE). The first class captures the instant of time when the received power exceeds a threshold (usually set depending on the background noise conditions), the second, instead, is based on the knowledge of the received echo direct model. In this second case, in fact, the functional dependence of the received waveform on the main parameters describing the scenario, including the height of the profile, is assumed to be known. Therefore, the actual measured data can be fitted by the echo model and the parameters of the scene are estimated so that the distance with the actual data is minimized. If the direct model of the echo is appropriate and accurate, the MLE method allows a more precise estimation of the height profile and, above all, allows to estimate other additional features of the surface under survey, as for instance its roughness.

Here we introduce, for the first time in the area of altimetry, a fractal-based direct model for simulating the radar altimeter echoes.

A fractal description for the sensed surface is employed; then, fractal scattering techniques are applied to estimate intensity and shape of the return

pulses. The model is appropriate for a large variety of natural surfaces, thus being not only innovative but also useful, in particular for deep space exploration where fractal models are usually adopted for Planets' surface modelling. The result is two-fold: this more accurate and reliable direct model for the altimeter echoes from one side may be the basis to design an improved inversion (MLE) method for estimating the surface profile; from the other side, proper processing of received echoes may provide more information on the sensed surface in addition to its simple height profile. This latter statement is based on the evidence that the width and the shape of the echoes contain value-added information (in addition to the simple height profile) about the topography of the scattering surface, information that is ignored by the TD method. This paper proceeds along this latter line. A new systematic procedure to compute the altimeter signal return is presented, thus showing the link between the signal return shape and most relevant surface topography features including height, slope, sub-surface layers and different scales of the illuminated footprint surface roughness. The analysis is supported by a validation step making use of some actual experimental data. Until now, exploitation of altimeter echoes based on physical models has only been available for some ocean surfaces: in this case the echoes are modelled in terms of some relevant sea state parameters [1]. Inversion of this model has been used to retrieve these parameters [2, 3]. However, the empirical data collected from many altimetry missions on solid surfaces (Cassini altimetry [4]) have shown that the received pulses exhibit more involved shapes than those predicted by Brown's model. This is not a surprise since the Brown model assumptions are not applicable to generic topography where the surface cannot be considered flat with a superimposed Gaussian roughness. In recent years, some new altimeter data models have been developed; however, these models do not make use of fractal surface models which have been shown to be appropriate for natural surfaces. As a matter of fact, it has been demonstrated [5, 6, 7, 8, 9] that fractal geometry is the only one suitable to reliably describe natural surfaces. Many of the natural mechanisms regulating surface evolution persist at different scales, so that natural surfaces exhibit auto-similarity and auto-affinity properties, as predicted by fractal models. In this dissertation more appropriate models for the surface representation and the coherent scattering mechanism are proposed; they are both based on the fractal geometry. As explained in the next Chapters, the band-limited fractional Brownian motion (fBm) model is used to represent the stochastic behaviour of the surface where appropriate surface realizations are generated by means of the band-limited Weierstrass-Mandelbrot (WM) func-

tion. In particular, it has been shown that the fBm model is appropriate for many natural surfaces on Earth [9, 10] and other planets in the Solar System [11, 12].

As a consequence of the surface description and the relative scattering computation a simulative model of the altimeter echoes has been implemented; in particular, reference is made, but is not limited, to the exploration of the natural satellite of Saturn, Titan, in the framework of Cassini mission (a joint NASA, ESA, ASI project conducted by the Space Agencies of United States, Europe and Italy, respectively) [4].

The presented direct model has been validated with the Cassini altimeter data. In fact, setting the simulation procedure at the same operating conditions of the Cassini Radar Altimeter, “quite similar” pulses have been generated. The potentiality of the model claims for the development of a rigorous inversion scheme, able to extract information on the surface under survey from the collected data. The inverse model is object of future studies. At the present, anyway, the proposed model can be very useful, because it can be used to generate an atlas of received echoes, thus helping to better understand the actual data. These ones in fact can be compared to the ones of the atlas and some precious value-added information about the scenario of interest can be inferred.

Chapter 1

Fundamentals

The goal of this chapter is to provide the key concepts necessary to fully understand the content of this dissertation. The first section introduces some basic definitions about the radar satellite altimetry and its applications. The second section describes the instruments to be used for the altimeter data processing. The third section is useful to correctly place this contribution in the appropriate scientific area; in fact, a brief qualitative summary of the most important results obtained since from the radar altimetry origins up to its recent developments is presented by means of an overview of the main Radar Altimetry missions.

1.1 Radar Satellite Altimetry Basics

The altimeter is an active sensor for remote sensing that measures the height of an object, typically an extended surface, above a fixed level. It estimates the vertical distance between the sensor (whose position above the reference is usually well known, as later on explained) and the surface, thus measuring, indirectly, the height of the surface of interest. The altimeter can work in the frequency range that spans from the microwaves up to the optical frequencies, being referred to as RADAR, *RA*dio *D*etection *A*nd *R*anging, and LIDAR, *L*ight *D*etection *A*nd *R*anging, altimeter, respectively. Moreover, the altimeter can be mounted on aircrafts or satellite platforms, depending on the applications of interest. The dissertation content is limited to the radar satellite altimetry.

The electromagnetic pulses are vertically transmitted by the Radar Altimeter (RA) antenna; they travel from the sensor towards the surface and back to

the satellite, where they are received. Altimetry satellites basically determine this distance.

However, it is worth noting that this is not the only measurement made in the process, and a lot of other information can be extracted from altimetry. The principle is that the altimeter emits a radar wave and analyses the return signal that bounces off the surface. Surface height is the difference between the satellite's position on orbit with respect to an arbitrary reference surface (the Earth's centre or a rough approximation of the Earth's surface: the reference ellipsoid) and the satellite-to-surface range (calculated by measuring the time taken for the signal to make the round trip). Besides surface height, by looking at the return signal's amplitude and waveform, it is also possible to measure wave height and wind speed over the oceans, and more generally, backscatter coefficient and surface roughness for most surfaces off which the signal is reflected. If the altimeter emits in two frequencies, the comparison between the signals, with respect to the frequencies used, can also generate interesting results (rain rate over the oceans, detection of crevasses over ice shelves, etc).

To obtain measurements accurate to within a few centimetres over a range of several hundred kilometres requires an extremely precise knowledge of the satellite's orbital position. Thus several locating systems are usually carried onboard altimetry satellites. Any interference with the radar signal also needs to be taken into account. Water vapour and electrons in the atmosphere, sea state and a range of other parameters can affect the signal round-trip time, thus distorting range measurements. It is possible correct these interference effects on the altimeter signal by measuring them with supporting instruments, or at several different frequencies, or by modelling them. Altimetry thus requires a lot of information to be taken into account before being able to use the data. Data processing is also a major part of altimetry, producing data of different levels optimised for different uses at the highest levels.

In the simplest scenario, it is possible to write the following relation¹:

$$h = H - r \tag{1.1}$$

where, as depicted in fig. 1.1:

- r is the range coordinate, the satellite to surface distance. Radar altimeters on board the satellite transmit signals at high frequencies, and receive the echo from the surface (the "waveform"). This is analysed to derive a precise measurement of the time taken to make the round

¹www.altimetry.info/

trip between the satellite and the surface. This time measurement yields a range r measurement (see next subsection for further details) being scaled to the speed at which electromagnetic waves travel. This speed is equal to the speed of light in the most of the path; only in the last part of the travel, in fact, the electromagnetic waves can be affected by the presence of a medium (the atmosphere, in the case of the Earth). Once these phenomena have been corrected for, the final range can be estimated with great accuracy (see next Subsection on data processing).

- H is the satellite altitude. The critical orbital parameters for satellite altimeter missions are period, inclination and altitude. The period, or ‘repeat orbit’ is the time needed for the satellite to pass over the same position on the ground, uniformly sampling the Planet’s surface. Inclination gives the highest latitude at which the satellite can take measurements. The altitude of a satellite (S) is the satellite’s distance with respect to an arbitrary reference (e.g. the reference ellipsoid, a rough approximation of the Planet’s surface). It depends upon a number of constraints (e. g. inclination, atmospheric drag, gravity forces acting on the satellite, area of the world to be mapped, etc). The satellite can be tracked in a number of ways so as to measure its altitude with the greatest possible accuracy thus determining its precise orbit, accurate to within few centimeters. Describing the used techniques is beyond the scope of this dissertation.
- h is the Surface height relative to the same reference of the satellite platform.

The range coordinate r varies along the satellite track, due to both the surface topography and the altimeter orbit above the origin of the coordinate system, as depicted in Fig. 1.2. Unfortunately, in a non-ideal scenario, the scattering surface is not made only by the point at sensor nadir. The altimeter looks at a portion of the surface, named footprint. Even in the best cases, the received echo is due to the superposition of the responses of each scatterer in the footprint. This affects the estimation of the range coordinate r , thus producing errors on the final estimate of the surface height.

A primary aspect in the sensor-surface height measurement error is the working condition of the altimeter, that affects the size of the illuminated area. The altimeter can work in a beam-limited or a pulse-limited mode. The difference is the way of limiting the portion of the area on the target-surface over which the range from the altimeter height to the reference surface is measured. The beam-limited footprint is defined to be the area on target surface within

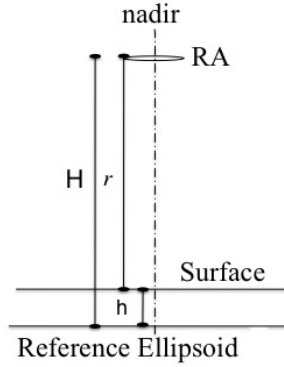


Figure 1.1: Geometry out of scale

the field of view subtended by the beam width of the antenna gain pattern. For a narrow-beam antenna, the antenna beam-width can be expressed as:

$$BW_{3dB} \cong \frac{\lambda}{L} \quad (1.2)$$

where λ is the operating wavelength and L is the linear size of the antenna in the considered direction. In particular, the *along-track* resolution and the *cross-track* resolution can be defined. Therefore the beam-limited footprint diameter becomes:

$$FP_{BL} \cong \frac{\lambda}{L} h \quad (1.3)$$

The pulse-limited footprint is limited by transmitting a very short pulse with duration of a few nanoseconds (pulse-limited configuration) from an antenna with a smaller diameter and correspondingly wider beamwidth. The illuminated area on the surface is therefore determined by the pulse-width instead of the beam-width. By simple geometric considerations we have:

$$fp_{PL} \cong 2\sqrt{ct\tau h} \quad (1.4)$$

Since the target-surface height (given by Eq. 1.1 relative to the reference ellipsoid) is the result of several geophysical effects and topographic characteristics, it is possible to demonstrate that the error made in the height measure is different depending on the operating mode of the altimeter. In particular,

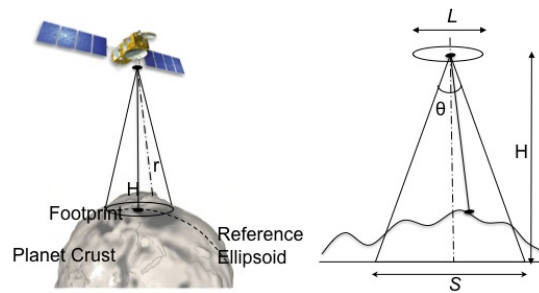


Figure 1.2: On the left, a 3D picture, out of scale, of the scenario with a visible surface topography; on the right a 2D section of the same scenario.

in presence of small slopes (i.e. the ocean surfaces) it is convenient to use a pulse limited altimeter, while in presence of large slopes a beam-limited one is preferred.

The accuracy required for the estimation of r , or equivalently h , is different depending on the applications of interest and, as a consequence, on the processing applied to the raw data. In the following subsection the basic aspects entering in the altimeter data processing are presented.

1.2 Standard Processing Techniques

In order to understand how the information of interest can be extracted from the altimeter raw data, two subsections are here proposed. The first explains the operating principle of the altimeter when the sensed surface is flat; the second evaluates the effects of introducing a topography, thus highlighting its consequences on the processing schemes to be adopted to obtain the desired information.

The altimeter raw data is the electromagnetic pulse received by the sensor. The information to be recovered is the round trip delay (then transformed into the distance from satellite to the ground, as before explained). There are two classes of methods that allow to obtain this information: *Threshold Detection* and *Maximum Likelihood Estimation* algorithms.

The first class of methods is very simple, because it does not require any kind of knowledge on the surface of interest. It is based on the capture of the instant of time when the pulse is received, i.e. when the received power exceeds a certain threshold, usually depending on the background noise.

The second class of methods, instead, requires the knowledge of the model of the received echo, that is the functional dependence of the pulse shape on the parameters describing the scenario of interest. The values of these parameters have to be found that minimize the distance with the actual data.

Obviously the effects of the topography are different depending on the class of method adopted for processing the data.

1.2.1 Ideal flat surface investigation

When the surface is flat and smooth the point at nadir is the closest one to the sensor; the received pulse leading edge arises (i.e. exceeds the set threshold) at the instant of time corresponding to the round trip time from the sensor to the nadir-point. Ideally, being the surface flat and smooth, the response of the whole surface coincides with the target-sensor impulse response. The received echo is only a shifted and scaled version of the transmitted pulse. In this case, both the processing classes, TD and MLE, are successful.

Unfortunately, totally flat and smooth surfaces do not exist in nature. Therefore, such a simplified scenario does not describe any possible actual case. In fact, even in the case of ocean surfaces, the sensed scenario is made by a macroscopically flat surface that is not smooth, characterized by an impressed roughness given by the capillary waves. In this scenario, the leading edge of the pulse represents the desired sensor-target distance, while the trailing edge is affected by the presence of the roughness. In fact the pulse does not go rapidly to zero, because the overall surface response is given by the superposition of the responses of all the scatterers present in the scene. In particular, due to the roughness, the power is backscattered in the sensor direction by a number of scatterers, different from the nadir point, at higher range distances, that are responsible for the pulse wide increasing, as it is visible from fig. 1.3, where an example of the actual pulses received by the Poseidon altimeter (see Sect. 1.3) is showed.

In cases like this, anyway, the information on the roughness of the surface is achievable. In fact, over an ocean surface, the echo waveform has the characteristic shape of fig. 1.4 that can be described analytically [1]. From this shape, six parameters can be deduced, by comparing the real (averaged) waveform with the theoretical curve:

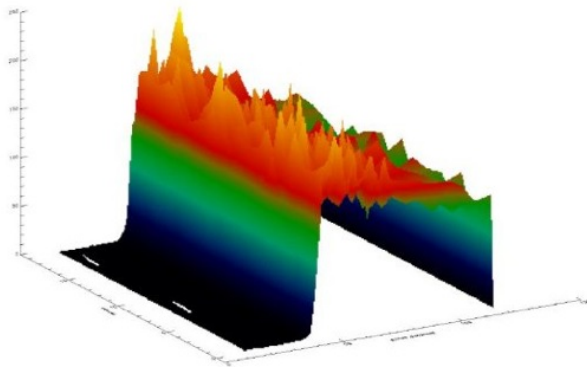


Figure 1.3: An example of waveform received on ocean surfaces, from Poseidon mission.

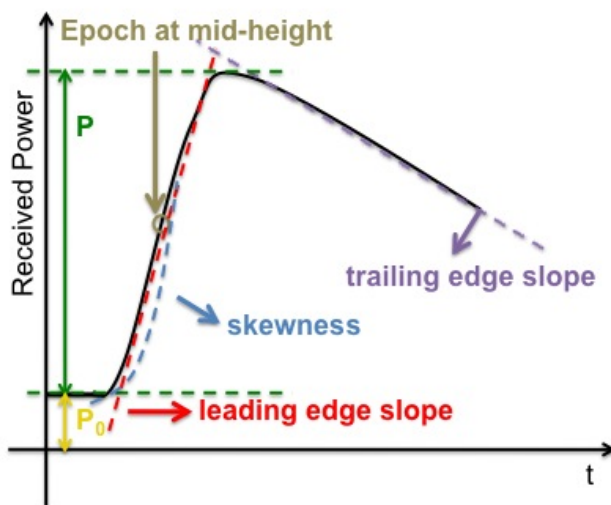


Figure 1.4: A typical waveform received on ocean surfaces.

1. epoch at mid-height: this gives the time delay of the expected return of the radar pulse (estimated by the tracker algorithm) and thus the time the radar pulse took to travel the satellite-surface distance (range) and back again.
2. P , the amplitude of the useful signal. This amplitude with respect to the emission amplitude gives the backscatter coefficient.
3. P_0 , the thermal noise.
4. Leading edge slope: this can be related to the significant wave height (SWH).
5. Skewness: the leading edge curvature.
6. Trailing edge slope: this is linked to any mispointing of the radar antenna (i.e. any deviation from nadir of the radar pointing) or to the surface roughness.

The radar altimeter receives the reflected wave (or echo), which varies in intensity over time. Where the sea surface is flat (a), the reflected wave's amplitude increases sharply from the moment the leading edge of the radar signal strikes the surface. However, in sea with high gravity waves, the electromagnetic wave strikes the crest of one wave and then a series of other crests which cause the reflected wave's amplitude to increase more gradually. It is possible to derive ocean wave height from the information in the reflected electromagnetic wave, since the slope of the curve representing the leading edge of the received power waveform is proportional to ocean wave height, [13].

1.2.2 Natural land surface investigation

More problems arise, instead, when the surface under survey is not flat. Surfaces which are not homogeneous, which contain discontinuities or significant slopes, such as some land surfaces, make accurate interpretation more difficult. This is mainly because there can be points into the footprint closer to the sensor than the nadir-point. The received pulse is in this case anticipated respect to the expected instant, and an error is committed in the nadir point height estimation. This is the reason why such a kind of scenario is particularly critical for adopting the TD processing scheme.

Unfortunately, the MLE algorithms also fail on land surfaces. This happens because a model of the echo received from land surfaces, as good as the

Brown's model for ocean surfaces, is not available. In fact, since the continental lands are composed of a very varying heterogeneous surfaces, the altimeter footprint is frequently composed of and contaminated by a multiplicity of surfaces. Thus, waveforms on these surfaces include a wide variety of configurations which are difficult to classify and process.

The problem is that, at least in principle, analyses from waveforms over heterogeneous surfaces should enable to retrieve several parameters and deduce other interesting characteristics. For example, the backscatter coefficient is useful to characterize the surface: a low value for mountainous regions and high value on flat surfaces or wetlands. The backscatter coefficient can also be related to the dates when a surface is completely frozen, when the ice breaks up, and fast-ice duration. The leading edge width is related to the penetration into the medium and the surface roughness of the target. The leading edge width values are high in desert areas due to the strong penetration of the wave and the dunes generated by the winds. Low values, related to weak penetration, correspond to dense vegetated areas, such as tropical or boreal forests, or to large river basins or flooded regions. As a consequence of these considerations the need arises for a model of the altimeter echoes able to describe all these aspects of the land surfaces, and, moreover, capable to provide information on some crucial topographic characteristics of the surface under survey, like its roughness at different scales of observations.

Due to the lack of such a complete model for land surfaces, the altimeters have been used so far only for monitoring the ocean surfaces, or at most for reconstructing the height profile of the land surfaces, thus renouncing to obtain value added information; this is detailed in Sect. 1.3.

1.3 Radar Satellite Altimetry Missions Overview

Seasat: Since the first dedicated altimeter was launched on *Seasat* platform (Fig. 1.5) in 1978, satellite altimetry importance and application fields have continuously increased. *Seasat* was managed by JPL and was launched into a nearly circular 800km orbit. Fourteen Earth orbits were completed each day, visible in Fig. 1.6.

Five complementary experiments designed to return the maximum information from ocean surfaces were onboard:

- Radar altimeter to measure spacecraft height above the ocean surface
- Microwave scatterometer to measure wind speed and direction



Figure 1.5: Seasat spacecraft, courtesy of NASA.

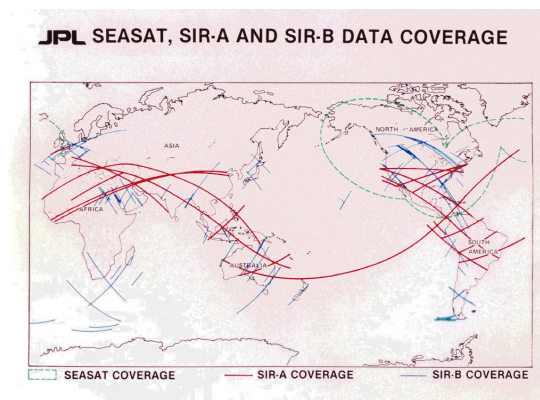


Figure 1.6: Earth coverage map, Seasat mission.

- Scanning multichannel microwave radiometer to measure sea surface temperature
- Visible and infrared radiometer to identify cloud, land and water features
- Synthetic Aperture Radar (SAR) L-band, HH polarization, fixed look angle to monitor the global surface wave field and polar sea ice conditions.

During Seasat operations, approximately 42 hours of data were collected. The mission was designed to demonstrate the feasibility of global satellite

monitoring of oceanographic phenomena and to help determine the requirements for an operational ocean remote sensing satellite system. Specific objectives were to collect data on sea-surface winds, sea-surface temperatures, wave heights, internal waves, atmospheric water, sea ice features and ocean topography. The mission ended on 10 October 1978 due to a failure of the vehicle's electric power system. Nevertheless, the mission demonstrated the feasibility of using microwave sensors to monitor ocean conditions, and laid the groundwork for future SAR missions. The major difference between Seasat-A and previous Earth observation satellites was the use of active and passive microwave sensors to achieve an all-weather capability.

Mainly, the evolution of the altimeter transmitter is marked by improvements in pulse compression techniques that have substantially reduced peak power requirements. Seasat operated at 1.275 GHz (L-band). All the altimeter missions below introduced operate at Ku-Band. The choice of frequency is constrained by both the system and operational requirements. Since a narrow transmitted pulse is required to achieve a reasonable range precision, high frequency operation will support both the large receiver bandwidth and narrow antenna beamwidth requirements. The upper limit on the operational frequency is constrained by atmospheric attenuation effects that significantly degrade the performance of the altimeter for frequencies $> 18\text{GHz}$. In some altimetric missions, for instance Topex, the radar altimeter instrument includes C-Band transmitter so that ionospheric propagation delays can be accurately measured. Generally, the two-frequency system will produce a sub-decimeter range precision so that very small variations (particularly in ocean surface) can be detected.

ERS: The first European satellite to carry a radar altimeter, ERS-1, was launched on 17 July 1991.

The European Remote Sensing satellite ERS-1, launched in 1991, carried a comprehensive payload including an imaging synthetic aperture radar, a radar altimeter and other powerful instruments to measure ocean surface temperature and winds at sea. ERS-2, which overlapped with ERS-1, was launched in 1995 with an additional sensor for atmospheric ozone research. At their time of launch the two ERS satellites were the most sophisticated Earth observation spacecraft ever developed and launched by Europe. These highly successful ESA satellites collected a wealth of valuable data on Earth's land surfaces, oceans, and polar caps and were called upon to monitor natural disasters such as severe flooding or earthquakes in remote parts of the world. Both ERS satel-

lites were built with a core payload of two specialised radars and an infrared imaging sensor. The two were designed as identical twins with one important difference: ERS-2 included an extra instrument to monitor ozone levels in the atmosphere. Shortly after the launch of ERS-2 in 1995 ESA decided to link the two satellites in the first ‘tandem’ mission which lasted for nine months. During this time the increased frequency and level of data available to scientists offered a unique opportunity to observe changes over a very short space of time, as both satellites orbited Earth only 24 hours apart. In March 2000, a computer and gyro control failure led to ERS-1 finally ending its operations, after far exceeding its planned lifetime. In July 2011, ERS-2 was retired and the process of deorbiting the satellite began.

This satellite was designed to have different orbital configurations. During the first few months, the Commissioning Phase, all instruments were calibrated and validated. Since then, ERS-1 has been flying two Ice Phases (in which the repeat period was 3 days), a Multi-Disciplinary Phase (a 35-day repeat orbit lasting from April 1992 till December 1994), and the Geodetic Phase, which started in April 1994 and had a repeat period of 168-days. The second repeat cycle in this Phase, till the launch of ERS-2, was shifted by 8 km with respect to the first, so a “336-day repeat” was obtained. ERS-2 was launched on 21 April 1995 and operated simultaneously to ERS-1, until ERS-1 was retired, in March 2000. Since their launch, ERS satellites have monitored the sea surface almost continuously. The accuracy of their altimeter range measurements has been estimated to be a little under 5 cm.

TOPEX/Poseidon: TOPEX/Poseidon was launched in 1992 as joint venture between CNES and NASA. While a 3-year mission was initially planned, with a 5-year store of expendables, TOPEX/Poseidon is still flying, 9 years after its launch. Due to the low orbit inclination, data coverage is more limited respect to ERS data. However, TOPEX/Poseidon is equipped with two experimental altimeters, one French and one US-made, that reach an accuracy in sea surface height determination around 3 cm. Thanks to this high performance, for the first time, the seasonal cycle and other temporal variability of the ocean have been determined globally with high accuracy, yielding fundamentally important information on ocean circulation.

Envisat: In November 2001, the European Space Agency launched Envisat, an advanced polar-orbiting Earth observation satellite which is still providing measurements of the atmosphere, ocean, land, and ice over a several year pe-

riod. The Envisat satellite has been designed to ensure the continuity of the data measurements of the ESA ERS satellites. A radar altimeter (RA-2) will be mounted on Envisat. This instrument is derived from the ERS-1 and 2 Radar Altimeters, providing improved measurement performance and new capabilities determining the two-way delay of the radar echo from the Earth's surface to a very high precision, within 2.5 centimetres.

Jason-1: Jason-1 is the first follow-on to TOPEX/Poseidon mission. It was launched in 2001 and provided highly accurate ocean altimetry data and near-real time altimetry data for predicting sea state and ocean circulation. Built by CNES, Jason is a lightweight altimeter based on the experimental secondary altimeter used by TOPEX/Poseidon. A second system at microwave has been used to measure the density of water vapour in the atmosphere, which allowed much more accurate atmospheric corrections. This system was able to measure sea surface height to within 2.5 centimetres.

CRYOSAT 2: CryoSat1 was the first satellite to be realized in the framework of the Earth Explorer Opportunity Missions of ESA's Living Planet Programme. The mission concept has been selected in 1999 with an anticipated launch in 2004. Cryosat 1 and following Cryosat 2 it is radar altimetry mission dedicated to observations of the Polar Regions. The goal is to study possible climate variability and trends by determine variations in thickness of the Earth's continental ice sheets and marine sea ice cover. The CryoSat2 Mission makes use of a near polar Low Earth Orbit (LEO) non sun- synchronous at an altitude of 720 km with an inclination of 92 degrees. The spacecraft accommodates the Altimeter SIRAL, DORIS receiver and Laser reflector.

In spite of the big progress done, big improvements can be achieved both for what concerns an increase in the range measurements accuracy, that could allow a more precise description of sea surface topography especially for regions where dynamic signals are not particularly strong (as the Mediterranean sea), or thinking of more reliable measurements near the coasts, and finally identifying sampling strategies that could allow a more synoptic and global coverage of the Earth surface which is fundamental for a precise monitoring of mesoscale currents.

The above excursus is focused on the application of the radar satellite altimetry on the Earth. This is not the only way of using the altimeter products. In fact, recently, altimeters are mounted on spacecraft and sent to explore the topography of other Planets in the solar system. Such a kind of application is

fascinating but very hard, because no additional geophysical information are available on other Planets, and every information achievable is really precious. In cases like these, it is crucial to be able to appropriately post-process the collected altimeter data thus trying to obtain value added information about the unknown surfaces. A very important example of this application is the

Cassini Huygens Mission: Cassini-Huygens¹ is one of the most ambitious missions ever launched into space. Loaded with an array of powerful instruments and cameras, the spacecraft is capable of taking accurate measurements and detailed images in a variety of atmospheric conditions and light spectra. Two elements comprise the spacecraft: The Cassini orbiter and the Huygens probe. In 2004, Cassini-Huygens reached Saturn and its moons. There the spacecraft began orbiting the system in July 2004, beaming home valuable data that will help us understand the vast Saturnian region. Huygens entered the murky atmosphere of Titan, Saturn's biggest moon, and descended via parachute onto its surface. Cassini-Huygens is a three-axis stabilized spacecraft equipped for 27 diverse science investigations. The Cassini orbiter has 12 instruments and the Huygens probe had six. Equipped to thoroughly investigate all the important elements that the Saturn system may uncover, many of the instruments have multiple functions. The spacecraft communicates through one high-gain and two low gain antennas. It is only in the event of a power failure or other such emergency situation, however, that the spacecraft communicates through one of its low-gain antennas. Three Radioisotope Thermoelectric Generators – commonly referred to as RTGs – provide power for the spacecraft, including the instruments, computers, and radio transmitters on board, attitude thrusters, and reaction wheels. In some ways, the Cassini spacecraft has senses better than our own. For example, Cassini can “see” in wavelengths of light and energy that the human eye cannot. The instruments on the spacecraft can “feel” things about magnetic fields and tiny dust particles that no human hand could detect. The science instruments can be classified in a way that can be compared to the way human senses operate. Your eyes and ears are “remote sensing” devices because you can receive information from remote objects without being in direct contact with them. Your senses of touch and taste are “direct sensing” devices. Your nose can be construed as either a remote or direct sensing device. You can certainly smell the apple pie across the room without having your nose in direct contact with it, but the molecules carrying the scent do have to make direct contact with your sinuses. Cassini's

¹www.nasa.gov

instruments can be classified as remote and microwave remote sensing instruments, and fields and particles instruments – these are all designed to record significant data and take a variety of close-up measurements.

The remote sensing instruments on the Cassini Spacecraft can calculate measurements from a great distance. This set includes both optical and microwave sensing instruments including cameras, spectrometers, radar and radio. The radar system has a precise temporization, working in different mode depending on the height of flight of the spacecraft. It can work in SAR, scatterometer or altimeter mode. The radiometer is always on.

The fields and particles instruments take “in situ” (on site) direct sensing measurements of the environment around the spacecraft. These instruments measure magnetic fields, mass, electrical charges and densities of atomic particles. They also measure the quantity and composition of dust particles, the strengths of plasma (electrically charged gas), and radio waves.

Chapter 2

Developments in radar altimetry

In the previous chapter the importance of appropriate direct models in the data processing has been highlighted as related to the main applications of the late radar altimetry. It turned out from the previous chapter that MLE results are strongly dependent on accuracy and reliability of the employed models. To this aim, a closed form analytical model is clearly needed, able to appropriately describe the altimeter raw data, to fit the experimental data, thus estimating the surface of interest characteristic parameters. In this Chapter the recent developments of the altimeter employed waveform models are reported and discussed. The chapter is organized in two sections: the first one describes the most important model developed in the field of altimetry, the Brown's model [1]. Its limitations are discussed. The second section shows the most recent studies developed in the field of altimetry after the Brown's model, how they have tried to overcome the reference model's limitations and where they succeed and/or fail.

2.1 The reference model of Brown

In order to understand the proposed model, it is important to analyze deeply the current reference models in the field of altimetry. The most important model used in the *classic* altimetry applications is the Brown's model [1]. This model has assumed a key role in the field of altimetry for its strength and simplicity. It is based on the convolutional model of Moore and Williams [14], subsequently modified by other authors [15, 16], and applied to the case of pulse-

limited radar altimeters. The key (and actually, critical) assumption of these approaches is about the completely incoherent nature of the scattering mechanism. This assumption is motivated in those papers by the roughness of the (ocean) surface at scales comparable to the electromagnetic wavelength: the echoes phase shifts from different points of the surface are seen as uniformly distributed independent random variables, so that power, and not amplitude summation is considered to be appropriate [14]. As a consequence, power, and not an amplitude impulse response of the radar-surface is computed in [1]. More specifically, in [1] the overall power impulse response (as function of the time), $h(\tau)$, of the radar-surface is modeled as the convolution of the radar system point target response $P_p(\tau)$ with the average surface impulse response $P_I(\tau)$:

$$h(\tau) = P_p(\tau) \otimes P_I(\tau) \quad (2.1)$$

with

$$P_I(\tau) = P_{FS}(\tau) \otimes P_h(\tau) \quad (2.2)$$

wherein $P_{FS}(\tau)$ is the average flat surface impulse response and $P_h(\tau)$ is the height probability density of the specular points, that is typically chosen with a Gaussian shape. Key hypotheses for this model are, among others, the presence of a scattering flat surface with a superimposed Gaussian roughness; the stationarity of the observed roughness; the variation of the scattering process along the whole scene due only to the possible change of backscattering cross section per unit scattering area σ^o (that is assumed to exhibit a Gaussian dependence on the incidence angle). Consequently, (for more details see [1]), the expression of the impulse response (normalized to the transmitted power) can be written in closed form as follows:

$$h(\tau) = A \exp \left[-\frac{c\tau}{h} \left(\frac{4}{\gamma} \cos(2\theta) + \alpha \right) \right] I \left(\frac{4}{\gamma} \sqrt{\frac{c\tau}{h}} \sin(2\theta) \right) \quad (2.3)$$

wherein:

- A is a factor that accounts for the antenna gain and the propagation, [s^{-1}].
- c is the speed of light, [m/s].

- γ is a dimensionless parameter related to the antenna beam (gaussian assumed);
- h is the altimeter altitude [m];
- θ is the off-nadir angle [rad];
- α is a dimensionless parameter that provides the dependence (with a prescribed Gaussian shape) of the backscattered power density on the incidence angle.
- I is a second kind Bessel function of order zero.

However, the empirical data collected from altimetry missions on solid surfaces have shown that the received pulses exhibit more involved shapes than those predicted by Brown's model [4]; this is motivated by the theoretical consideration that the Brown's model assumptions are not applicable to a generic topography, because the surface cannot be always considered flat with a superimposed Gaussian roughness. In addition the assumption of an incoherent scattering mechanism is questionable too: for solid surfaces possible coherent effects must be taken into account for a microwave radar. Several models have been developed in the last decades in order to overcome the strong limitations of the Brown's model.

2.2 Recent Developments

The main limitation of the Brown's model is due to the assumption made on the sensed surface. In fact, the most of the natural surfaces cannot be appropriately described by a gaussian model of roughness. The reason is that forces that model natural surfaces, like gravity and microgravity, tensions, frictions, vibrations, erosions, thermal and freezing gradients, chemical reaction, etc, and periodic and a-periodic happenings, like seasons and vegetation changes, sun, wind, rain, snow, slides, subsidence, etc. generate surfaces whose topological dimension is larger than 2; i.e., larger than the Euclidean one. Loosely speaking, the corrugations and microondulations impressed by the natural forces tend to expand the surface into the surrounding volume, thus "extending" its topological dimension in the range from 2 (Euclidean surface) to 3 (Euclidean volume). Such a geometry is well described by the fractal geometry, which considers surfaces whose topological dimension is equal to $D = 3 - H$,

$0 < H < 1$ being the Hurst exponent. The conclusion is that natural surfaces need to be modeled by an “ad hoc” geometry, the fractal one [5, 6, 7, 8, 9].

As a consequence of the above considerations, in this dissertation a model of the altimeter data is introduced, based on fractal assumption of the sensed surface. The model is detailed in its mathematical and physical aspects in Sect. 4.

Previously some authors have sometimes introduced the fractals in the field of altimetry, but without having the perspective to develop an inversion scheme to retrieve much more than a surface profile from the altimeter data. This enlarged application of the altimeter was sometimes claimed but never fully reached: this was due to the inappropriate choice of the surface and radar models that were previously employed.

In particular, in [17, 18] fractals are used in order to describe ocean surfaces, at small scales only, while in this work the fractal geometry is used, more generally, to represent landscape surfaces, by means of a multi-scale model. Moreover, in [17, 18] there is no effort to relate the received waveform shape to the fractal parameters of the scene. The present novel proposal for a full fractal approach (surface and radar model) can help developing inverse schemes to reach this ambitious goal. As above explained, exploitation of altimeter echoes based on physical models has only been available for some ocean surfaces: in this case the echoes have been modelled in terms of some relevant sea state parameters [1]: inversion of this model has been used to retrieve these parameters [2, 19, 20, 21, 22, 23, 24]. However, the empirical data collected from many altimetry missions on solid surfaces (Cassini altimetry [25, 26]) have shown that the received pulses exhibit more involved shapes than those predicted by Brown’s model [3, 27]. This is not surprising since the Brown’s model assumptions are not applicable to generic topographies where the surface cannot be considered flat with a superimposed Gaussian roughness. In addition, as said before, the Brown’s model assumes an incoherent scattering mechanism, and this is certainly questionable for solid surfaces where possible coherent effects must be taken into account for microwave radar illumination. During the last years other authors have tried to associate the altimeter return waveform shapes to surface parameters, for both the ocean and ice-sheet or coastal cases; but these works are not based on physical models of the landscape surfaces. This makes impossible to retrieve any additional information about the sensed surface from the echoes analysis [28, 29, 30, 31]. Recently, several altimeter data models have been developed [32, 33, 34, 35, 36, 37, 38] for landscape altimetry. In particular, in [35] a deep exploration of the scattering from land-

scape and ice-sheet surfaces is presented. Direct and inverse problems are dealt with and the scattering computation involves surface and volumetric contributions. The resulted direct model has been simplified and linearized in order to be inverted, but, obviously, some approximations have been made. The result is the generation of several limitations on the scattering model that are not always true for any kind of landscape scene. Moreover, classical model are there used for surface description, thus not taking into account the self-affinity characteristics intrinsically associated to natural landscapes. In fact, the employed models do not make use of fractal geometry, which, as already stated, has been shown to be the most appropriate for natural surfaces, both ocean [17, 18] and terrain ones [7, 8, 9, 17]. As a matter of fact, it has been demonstrated that fractal geometry is the more suitable to reliably describe natural surfaces [5, 6, 7, 8, 9]. Many of the natural mechanisms regulating surface evolution persist at different scales, so that natural surfaces exhibit auto-similarity and auto-affinity properties, as predicted only by the fractal models.

This more accurate and reliable direct model for the altimeter echoes may be the basis to design, in future works, an improved inversion (MLE) method for estimating the surface profile, that could provide not only a more accurate estimate of the landscape height profile but also additional information on the sensed surface, including slope, sub-surface layers, different scales of the illuminated footprint surface roughness, modeled by means of fractal parameters.

Chapter 3

Natural surfaces and fractals

In this chapter the fundamentals of fractal geometry are provided, being the basis to understand the proposed model detailed in the Sect 4. In particular, appropriate models for the description of natural terrain surfaces are presented.

Fractal models are widely considered the most appropriate to quantitatively describe natural surfaces. In fact, fractal geometry is able to simply account for the non-stationarity of natural surfaces, as well as for their self-affinity [5, 6, 7, 8, 9].

A fundamental concept of fractal geometry is the Hausdorff- Besicovitch (HB) dimension, or fractal dimension. The definition of HB dimension is based on the concept of the Hausdorff measure. A set is said to be fractal if its fractal dimension is greater than its topological one. For instance, a surface is fractal if its fractal dimension D is greater than 2. The fractal dimension is related to the surface roughness: an almost smooth surface has a low (i.e., slightly greater than 2) fractal dimension, whereas an extremely rough surface has a fractal dimension that approaches 3, since it tends to fill a volume. All fractal sets exhibit some form of scale invariance. We recall that a set is self-similar if it is invariant (possibly in statistical sense) with respect to a transformation in which all the coordinates are scaled down by the same factor; it is self-affine if it is invariant (possibly in statistical sense) with respect to a transformation in which coordinates are scaled down by factors not all equal. As already stated, self- affinity of fractal sets is the key property that makes them particularly useful in describing natural surfaces. These fundamental properties of natural surfaces are hardly reproduced by classical surface models based on Euclidean geometry. In particular, the second order statistical characterization of the surface can be very inaccurate, if use is made of classical concepts

as the correlation length: in fact, the lack of a characteristic scale is a key feature of natural profiles, well-known, for example, to earth science researchers. For scattering evaluation purposes a second order characterization of the surface is necessary [9]. In the fractal case this kind of description is very simple and straightforward, while in the classical case a heuristic choice of the shape of the correlation function has to be performed. The success of fractal geometry in describing natural scenes is also due to the existence of scattering models based on such a description for the surface. It has been demonstrated that the use of fractal scattering models strongly improves the performance in the evaluation of the scattered field.

The Chapter is organized as follows: in Sect. 3.1 an introduction to the fractal models used throughout the Thesis is provided. The Section 3.2 defines and details the main properties of the fBm stochastic process. In Sect. 3.3 another fractal process is presented, the Weierstrass Mandelbrot fractal function. The connection between the fBm and the WM models is explained in the last Section 3.4.

3.1 Fractal description of natural surfaces

Many different types of fractal functions have been used in literature to describe and synthesize natural surfaces [5, 6, 7, 8, 9], [39]. A deep examination of all the possible methods is beyond the scope of this chapter, that aims to provide the instruments to fully understand the author's proposed model. Therefore, to this dissertation purposes, the ways to describe natural surfaces come to be essentially two.

The first method is to describe the surface as a realization of a fractional Brownian motion (fBm) stochastic process. In this case, it is possible to obtain a very simple expression for the mean square value of the field, depending on the fractal parameters of the surface. Conversely it is not possible to compute the (complex) field [9].

Another way to describe fractal surfaces is using the Weierstrass- Mandelbrot (WM) function. The main advantage of using the WM function is that it is possible to obtain an analytical expression of the (complex) scattered field. However, the obtained expression is very involved, and it is not possible to analytically evaluate the (expected) scattered power density [9]. In this work the mean square value of the backscattered, which, apart from multiplicative factors, is equal to the Radar Cross Section (RCS), is of interest. Hence, an fBm description of the surface is employed: however, in practical cases fBm

surfaces are better synthesized through appropriate techniques based on the use of the WM function. Thus, in the following both WM and fBm surface models are considered; conversely, the scattering problem is addressed only starting from an fBm description for the height profile.

3.2 Fractional brownian motion process

The fBm is defined in terms of the probability density function of its height increments: a stochastic process $z(x, y)$ may represent an isotropic fBm surface if, for every (x, y, x', y') it satisfies the relation:

$$\Pr \{z(x, y) - z(x', y') < \xi\} = \frac{1}{\sqrt{(2\pi)s^2 l^{2H}}} \int_{-\infty}^{\xi} \exp\left(-\frac{\zeta^2}{2s^2 l^{2H}}\right) d\zeta, \quad (3.1)$$

where:

- H , the Hurst coefficient or exponent, ranges in the interval $[0, 1]$ and is related to the fractal dimension $D = 3 - H$;
- s , the incremental standard deviation (a real value measured in $[m^{(1-H)}]$), is related to the characteristic length of the fBm surface, the topothesy T , by the relation $s = T^{(1-H)}$;
- T , the topothesy, is the distance over which chords joining points over the surface have a *root-mean-square* (rms) slope equal to unity;
- l represents the distance on the (x, y) plane between the points (x, y) and (x', y') .

For a given surface the structure function (whose plot is named the variogram), $V(l)$, is defined as the mean square increment of elevation points placed at distance l :

$$V(l) = \left\langle (z(x, y) - z(x', y'))^2 \right\rangle \quad (3.2)$$

The structure function of an fBm surface can be evaluated in terms of the parameters H and s as:

$$V(l) = s^2 l^{2H}. \quad (3.3)$$

Eq. 3.3 can be written in logarithmic form as:

$$\log V(l) = 2\log s + 2H\log l, \quad (3.4)$$

which defines in a log-log plane a linear behavior with slope $2H$, and ordinate intercept $2\log s$. Due to the non-stationarity of the process, the evaluation of the spectrum is not a trivial issue [40]. Using mathematical instruments as Generalized Fourier Transforms and spatial-scale analysis (for example using wavelet theory), it has been demonstrated [9],[40] that the spectrum $S(k)$ of an isotropic fBm process exhibits a power law behaviour:

$$S(k) = S_0 k^{-\alpha}, \quad (3.5)$$

wherein the spectral and spatial domain parameters are related by the following relationships:

$$\alpha = 2 + 2H = 8 - 2D, \quad (3.6)$$

$$S_0 = s^2 2^{2H} 2\pi H \frac{\Gamma(1+H)}{\Gamma(1-H)}, \quad (3.7)$$

$\Gamma(\cdot)$ being the Gamma function. From the inequalities $0 < H < 1$ we get $2 < \alpha < 4$, which defines the range of allowed values for the spectral slope α . Note that also the spectral equation (3.5) provides a linear relation in a $(\log(S), \log(k))$ plane, with parameters related to those of the log-log representation introduced for the variogram. It is important to note that a surface satisfying Eq. (3.1) for every l is self-affine on all scales, so that it has details on any arbitrarily small scale and is not differentiable at any point (although it is continuous). Therefore, it cannot be used in electromagnetic scattering problems because the continuity conditions of tangential fields cannot be enforced. Furthermore, such surface is not stationary and suffers from the infinite variance problem (the integral of the power spectrum diverges in the low-frequency range), infrared catastrophe, if $\alpha > 2$, see Eq. (3.5). Such a surface is also called a mathematical fBm surface. However, natural surfaces exhibit a fractal behavior only on a wide but limited range of scales. In addition, the range of scales of interest for a scattering problem is limited on one side by the finite linear size L of the illuminated surface, and on the other by the fact that surface variations on scales much smaller than wavelength λ do not affect the scattered field. Accordingly, we consider physical fBm surfaces, i.e., surfaces that satisfy Eq. (3.1) only for $l_{\min} < l < l_{\max}$, with l_{\max} on the

order of L and l_{\min} on the order of $\lambda/10$. If $l_{\min} < l_{\max}$, this implies that such surfaces satisfy Eq. (3.5) only in a wide but limited range of spatial frequencies $k_{\min} < k < k_{\max}$, with $k_{\min} = \frac{1}{l_{\max}}$ and $k_{\max} = \frac{1}{l_{\min}}$. That is why these surfaces are also referred to as band-limited fBm. It can be demonstrated that band-limited fBm surfaces are stationary (at least in wide sense) and regular. Starting from the definition of such physical fractals is possible to find closed form expressions relating the fractal parameters to some equivalent classical parameters as variance, slope and curvature [9].

3.3 Weierstrass-Mandelbrot function

Among several possible representations of the WM function, one in particular is convenient for modeling the interaction of natural surfaces and electromagnetic waves [7], [41]. We may consider the non-normalized WM function $z(x, y)$ as the superposition of an infinite number of sinusoidal tones, each one characterized by the value of the index p :

$$z(x, y) = B \sum_{p=-\infty}^{+\infty} C_p \nu^{-Hp} \sin [k_0 \nu^p (x \cos \Psi_p + y \sin \Psi_p) + \Phi_p], \quad (3.8)$$

wherein:

- B [m] is the overall amplitude scaling factor;
- p is the tone index;
- k_0 [m^{-1}] is the wavenumber of the fundamental sinusoid ($p = 0$);
- $\nu > 1$ is the seed of the geometric progression accounting for the spectral separation of successive sinusoids;
- C_p, Ψ_p, Φ_p are the deterministic or random coefficients representing amplitude, direction and phase of each sinusoid. If the coefficients C_p are deterministic, they must be all equal and constant, so that the tone amplitudes, $BC\nu^{-Hp}$ ensure the correct power-law spectral behavior of the fractal function. For random coefficients C_p , the usual choice for their pdf is Gaussian with zero mean and unitary variance. If the coefficients Ψ_p s are deterministic, all equal and constant $\Psi_p = \Psi$, the surface exhibits the fractal behavior only in the direction selected by Ψ

(and is constant along the direction orthogonal to it). If, on the contrary, these coefficients are uniformly distributed in $[-\pi, \pi)$, the WM function is isotropic in the statical sense; any other choice leads to anisotropic surfaces. In this dissertation the WM surface is assumed isotropic. A different choice can be made in order to extend the content of this contribution to the case of anisotropic surfaces. This point can be subject of future developments. If the coefficients Φ_p are deterministic, they are usually selected to ensure that the WM function exhibits the self-affine behavior. If the coefficients Φ_p are random, they are usually chosen uniformly distributed in $[-\pi, \pi)$, and the zero-set of the WM function (i.e., the set of points of intersection with the plane $z = 0$) is nondeterministic.

In case of a random WM function, the random coefficients, C_p , Ψ_p and Φ_p , are usually assumed to be mutually independent. Equation (3.8) exhibits a non-integer fractal dimension D as soon as ν is irrational and the Hurst exponent is related to the fractal dimension D as

$$D = 3 - H. \quad (3.9)$$

In case of random coefficients, the WM function holds the self-affine behavior only for a scaling factor $r = \nu^n$. Whenever ν tends to 1 the WM function approaches the self-affine behavior in the statistical sense. A physical WM function can be obtained by just limiting the summation extent to P tones, thus obtaining band-limited WM surfaces:

$$z(x, y) = B \sum_{p=0}^{P-1} C_p \nu^{-Hp} \sin [k_0 \nu^p (x \cos \Psi_p + y \sin \Psi_p) + \Phi_p], \quad (3.10)$$

As in the case of fBm, use of band-limited WM surfaces is physically justified by the fact that any scattering measurement is limited to a finite set of scales. Let (X, Y) be the antenna footprint over the surface. The lowest spatial frequency of the surface, $k_0/(2\pi)$, is linked to the footprint diameter $\sqrt{(X^2 + Y^2)}$, while the upper one $k_0 \nu^{(n-1)}/(2\pi)$ is related to the electromagnetic wavelength λ , possibly through an appropriate safety factor χ in the range $[0, 1]$, usually set equal to 0.1. Accordingly, we can set

$$k_{\min} = k_0 = \frac{2\pi}{\sqrt{X^2 + Y^2}}, \quad (3.11)$$

$$k_{\max} = k_0 = \frac{2\pi}{\sqrt{\chi^\lambda}}, \quad (3.12)$$

Relations (3.11) and (3.12) can be used to determine the number of tones P needed to effectively describe the physical WM of interest:

$$P = \left\lceil \frac{\ln \left(\frac{\sqrt{(X^2 + Y^2)}/\sqrt{\chi^\lambda}}{\ln \nu} \right) \right\rceil + 1, \quad (3.13)$$

where the $\lceil \cdot \rceil$ operator is the ceiling, defined so as to take the upper integer of its argument.

Also in this case it is possible to obtain a relation between the parameters of the WM function and classical surface parameters [9].

3.4 Connection between WM and fBm surfaces

As a matter of fact, it is not trivial to obtain realizations of fBm sample functions characterized by H and S_0 parameters; conversely, the WM function is easily computed via simple summation of sinusoidal tones. For this reason it is useful to establish a relation between the fBm and the WM parameters in such a way that an fBm surface can be synthesized via an opportune WM function. As for the Hurst parameter, it is simple to verify that it is equal to the H value in (3.8): hence, we need only a relation for the amplitude factors S_0 and B .

Looking at Eq. (3.8), it can be noted that, under some hypotheses, the WM could be intended as a sampled representation of an fBm. Hence, the required connection can be established by comparing the corresponding power spectra and checking to what extent the former is a sampled representation of the latter at the discrete spatial frequencies $k_p = k_0 \nu^p$.

Dividing the spectral plane (k_x, k_y) into concentric annular regions of radii $(k_p \nu^{1/2}, k_p \nu^{-1/2})$ respectively, and computing the spectral power within each annular region pertinent to WM and fBm surface description, is possible to obtain the following relations involving the parameters of interest [9]:

$$B^2 = \frac{S_0}{2\pi H} k_0^{-2H} (\nu^H - \nu^{-H}), \quad (3.14)$$

which for ν approaching 1 (i.e., when the spectrum of the WM becomes almost continuous) can be written as:

$$B^2 = \frac{1}{\pi} S_0 k_0^{2H} (\nu - 1). \quad (3.15)$$

Summarizing, we can say that the WM function and the fBm process both possess the same Hurst parameter and hence, at least in the limit $\nu \rightarrow 1$, the same fractal dimension. This is consistent with the fact that the equivalent power spectral decay of the WM function and the power spectral decay of the corresponding fBm process are the same. Finally, if B is selected according to Eq. (3.14), then the power content of the WM function and the equivalent fBm process are equal on appropriate spectral intervals; in the limit of $\nu \rightarrow 1$ this last result is valid on any spectral interval.

Chapter 4

Fractal Based Model of Altimeter Data

In this chapter, as mentioned before, a new model is derived [43, 44, 45, 46, 47], that takes into account of heterogeneous topographies on natural terrains. This model introduces the description of the surface of interest in a new way, by considering different descriptions at different scales of observations and implements the relative scattering mechanisms. Transmitted waveform simulation and the sensed surface model are presented afterwards. In particular, in the first section the rationale of the overall echo model is presented; in the second section the adopted transmitted waveform modeling is detailed; the third section explains the choices made on the surface description, while the last section reports the electromagnetic scattering computation.

4.1 The rationale of the proposed approach

The proposed innovative logic scheme for the radar altimeter return computation is totally based on a fractal assumption, that enters at three different key stages as detailed hereafter.

1. Surface description.

We model the surface via an fBm (fractional Brownian motion) model, the best one to describe natural landscapes, as detailed in the previous chapter, [5, 6, 7, 8, 9]. We can, in principle, apply this model to any surface (spatial) scale involved in the altimeter acquisition thus ranging from (a certain fraction of) the radar wavelength (that is the minimum

scale to which the radar is sensible [9]), to the length of the acquired profile. However, the operational mode typical of a radar altimeter suggests us introducing appropriate (spatial) scales that can lead to efficient fractal representations of the sensed surface. In fact, the echoes received by the altimeter are usually sampled at a prescribed rate (each sample being termed range bin): surface portions (microscopic scales) that contribute in a single range bin can be efficiently described “on average” via some stochastic parameters, whereas surface description at larger scales (macroscopic scales) must be accomplished “in detail” generating appropriate specific realizations of the sensed area. Accordingly, we propose a composite, formally scale-dependent, fractal model to efficiently describe the surface roughness at both the microscopic and macroscopic scales.

- At the microscopic scales we stochastically represent the surface shape via a regular stochastic fractal fBm process.
- At the macroscopic scales we generate the surface realizations via a predictable stochastic fractal process, the WM (Weierstrass Mandelbrot) [9], [41] function, whose parameters can be set in order to warrant the equivalence to an fBm process, see Chapt. 3.

It is convenient to here underline that the macroscopic scale can be conveniently split into two scales according to the altimeter operational mode. As a matter of fact, the altimeter receives one echo for each transmitted pulse, whereas the collection of all the echoes received during an entire altimeter acquisition determines the radargram: accordingly, the surface portions contributing in one single received echo identify the footprint scale, whereas larger surface scales (profile scales) contribute to determine the entire radargram. For the sake of simplicity we consider the same fractal parameters at microscopic and macroscopic scales, but this hypothesis can be trivially relaxed if the case.

2. Scattering computation.

A facet scattering model is adopted to evaluate each altimeter echo. Roughness of each facet is provided by the microscopic scales and facet dimensions are selected so that scattering from each facet contribute to one range bin which is determined by the (mean) distance between the facet and the radar. Scattering from each facet is then computed via the solution of the fractal PO (Physical Optics) scattering method [9], (see

next section for details): this method is specifically conceived for fBm roughness at microscopic scales. Use of this (very much appropriate, [9]) scattering model is totally new within the altimeter modeling. Facet centers and orientations are determined by the macroscopic profile (determined via a WM function whose parameters can be linked to those of the fBm one) and the altimeter echo is computed by appropriately delaying in time domain the radar returns from all the facets that are present in the radar footprint. It is worth noting that no other use of fractal scattering models [9] that also present the above mentioned role of fractal microscopic and macroscopic scales can be found in the open literature on altimetry.

3. Discussion about the computed return.

Thanks to the fractal approach explained in the previous points, an innovative discussion is possible about the computed radar returns: this discussion can be based on the revealed (direct) connection between the fractal parameters of the scene and the echo shapes. This connection is for the first time presented in this paper, along with the rationale to apply it to compute the altimeter radargrams, and then also this discussion is new. In addition, by exploring the link we compute between the radar echoes and the fractal parameters of the scene, also the sensor performance can be evaluated in terms of sensibility to the fractal parameters variations. This step is propaedeutic to the design of an appropriate inversion framework, whose full setting is out of the scope of this work. Its exploration should necessarily start from the results of the present paper, and will be explored in the near future.

In the subsequent sections the details of the implemented model are presented.

4.2 Waveform Modeling

In most practical cases the altimeter transmitted waveform is a chirp-modulated signal. This is the case considered here, along with the use of standard processing of the chirped waveform. This choice comes from the chance offered by the NASA, to process the altimeter data collected by the Cassini-Huygens spacecraft. A linear frequency modulated chirp (with pulse length τ , chirp rate 2μ and bandwidth approximately equal to frequency de-

variation $\Delta f\tau/\pi$) at radio-frequency $\omega = 2\pi f$ is described (in phasor format), but for an irrelevant constant, by

$$f(t) = \text{rect} \left[\frac{t}{\tau} \right] e^{j\mu t^2} e^{j\omega t}, \quad (4.1)$$

t being the time variable. The received signal is given by the superposition of the radar returns, differently scaled in amplitude and differently shifted in time, for each point of the sensed surface. After the heterodyne process and the chirp compression the received signal is given by [48]:

$$g(t) = \int \int_S \gamma(x, y) \exp(-2jkr(x, y)) \text{sinc} \left(\pi \frac{t - 2r(x, y)/c}{2\Delta r(x, y)/c} \right) dx dy. \quad (4.2)$$

r being the distance between the platform and the generic point of the illuminated surface S , $\gamma(r)$ the reflectivity function accounting for the scattering properties of the surface, (as detailed in the Sect. 4.4), $k = \omega/c$, Δr being the radar range resolution, equal to $\frac{c}{2\Delta f} = \frac{\lambda f}{2\Delta f}$. It is worth noting that the evaluation of spatial integration variable r requires the surface to be modeled. Its reliable computation as function of cartesian coordinates, detailed in the next Sect. 4.3, requires modeling of both the surface roughness and the planet mean curvature.

4.3 Surface Modeling

One single model to describe the overall surface shape is not available. Thus, we introduce a simple smooth model for the mean planet surface and superimpose to this model any roughness that plays a significant role in the computation of the altimeter received echoes, see. Eq (4.2). For the sake of simplicity, the planet mean surface (curvature) is here assumed as a sphere S_T whose radius is indicated in the following as R_T ; generalization to more sophisticated ellipsoid-based models are simple. As mentioned above, the surface roughness must be precisely modeled at different scales; this is also confirmed by the simulation results reported in Chapt. 5. The above mentioned wavelength, footprint and profile spatial scales are hereafter detailed, and their role is clarified.

- *Wavelength scales*, include scales whose dimensions are comparable to the transmitted signal wavelength, thus entering in facets scattering eval-

uation (see Sect. 4.4), and extends to surface portion that contributes in one single range bin of each altimeter echo.

- *Footprint scales*, include scales comparable to the antenna footprint, defined by the antenna beamwidth and the platform height. More specifically, the minimum horizontal distances involved at this scales are considered such that the surface details are detectable from the radar, i.e. can be vertically resolved by the altimeter; the maximum horizontal distances involved at this scale are comparable to the footprint.
- *Profile scales*, involve dimensions comparable to the altimeter acquired profile. The minimum involved distance is that between two successive altimeter acquisitions. The maximum involved distance is the length of the entire acquired profile.

Altimeter data should provide the required information at profile scale. For each transmitted pulse (or set of pulses, if more pulses are combined to create a burst) along the altimeter path, the roughness at the profile scale is what determines the surface height with respect to the planet surface. Moreover, the microscopic roughness at wavelength scale enters only in the phase term in Eq. (4.2). Hence, in the following discussion we concentrate on the role of the macroscopic roughness whereas the model for the microscopic contribution is detailed later on in this Section. Fig. 4.1 shows the geometry of the problem. To simplify the drawing, only one section of the original three-dimensional geometry (including the sensor position and the corresponding nadir direction) is depicted; the figure is composed of two parts devoted to illustrate the rationale of our surface modeling.

In Fig. 4.1a the reference surface for the surface roughness at footprint scale is the plane $z = 0$, while in Fig. 4.1b is the sphere S_T . The meaning of the symbols introduced in Fig. 4.1 is:

- the \hat{z} axis is aligned to the sensor nadir direction and is pointing toward the sensor, then, $z = 0$ is the tangent plane to the reference sphere at the sensor nadir point;
- (x, y) locates the generic point, P , of the illuminated surface in the Cartesian coordinate system.
- h is the altitude of the altimeter platform over $z = 0$;
- $\beta(x, y)$ and $\Delta h(x, y)$, both indicate the effect of the planet curvature away from the nadir point, where

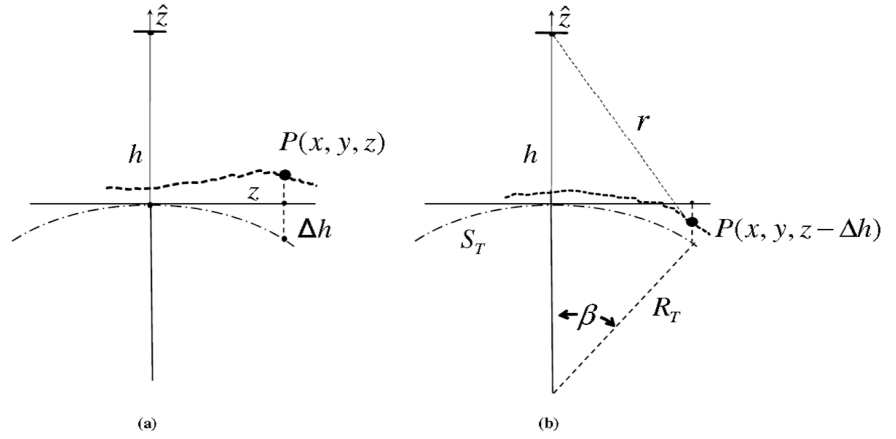


Figure 4.1: Section (out of scale) of the geometry of the system relevant to the problem: the reference surfaces are depicted. In (a) the reference surface is the plane $z = 0$, tangent to the planet, whose profile is described by $z(x, y)$, without taking into account the planet curvature whose shape is only indicated, but plays no role in the profile definition; in (b) the reference surface is the planet ideal shape, the sphere S_T , and the planet profile is described by $[z(x, y) - \Delta h(x, y)]$, thus taking into account the planet curvature.

$$\beta(x, y) = \arcsin \left(\sqrt{(x^2 + y^2)}/R_T \right), \quad (4.3)$$

and

$$\Delta h(x, y) = R_T \{1 - \cos [\beta(x, y)]\}, \quad (4.4)$$

In view of the above considerations, we can set $h'(x, y) = h + \Delta h(x, y)$, and we are now in position to simply express the distance τ , appearing in Eq. (4.2), from the altimeter platform to the generic point of the surface. Ignoring, for the time being, the curvature of the planet, the surface coincides with the tangent plane, $z = 0$, corrupted by the macroscopic roughness: accordingly, the surface generic point is indicated by $P(x, y, z)$, z being the macroscopic height coordinate over the plane $z = 0$ (Fig. 4.1a). This macroscopic height

can be deterministic, for instance a sinusoidal profile, or stochastic at macroscopic scale, or even a combination of the two. The planet curvature is now introduced: we deform the planar surface to the spherical one: accordingly, the new coordinates of the generic point are, $P(x, y, z - \Delta h)$. Then, the distance of the point P to the satellite position is (Fig. 4.1b)

$$r = \sqrt{x^2 + y^2 + [h - (z - \Delta h)]^2} = \sqrt{x^2 + y^2 + (h' - z)^2} \quad (4.5)$$

This model is introduced because it allows us to refer the surface roughness $z(x, y)$ to a reference plane $z = 0$ in a Cartesian coordinate system, and in this case reliable fractal or non fractal models are available for it. These models are both analyzed in the following.

Also the microscopic roughness at wavelength scale can be now modeled, by superposing the microscopic roughness, $z'(x, y)$ over the macroscopic one. With reference to Eq. 4.2 it is noted that the macroscopic roughness plays a significant role in all the factors appearing in the integral. On the contrary, the microscopic roughness is only relevant in the phase term of the exponential factor because it is of the same order of magnitude of the radar wavelength. Thus the processed signal is:

$$\begin{aligned} \tilde{g}(t/2c) = \\ \tilde{s}(r') \int \int_S \gamma(x, y) \exp(-2jkr(x, y) - z') \operatorname{sinc}\left(\pi \frac{r' - r(x, y)}{\Delta r(x, y)}\right) dx dy, \end{aligned} \quad (4.6)$$

where:

- $\gamma(r)$ is the square root of the backscattering coefficient [see subsequent Eq. (4.7)]; it accounts for the intensity of the scattered field;
- $r' = \frac{ct}{2}$;
- $\exp[-2jk(r_0 - z')] \operatorname{sinc}[\pi(r' - r_0)/\Delta r]$ represents (but for an ignored constant) the unit impulse response of the system depicted in Fig. (4.2), i.e., the signal that would be received as result of a transmitted chirped pulse scattered by a unitary point target $\gamma(r) = \delta(r - r_0)$ on the surface at $r = r_0$, followed by coherent demodulation and chirp processing.

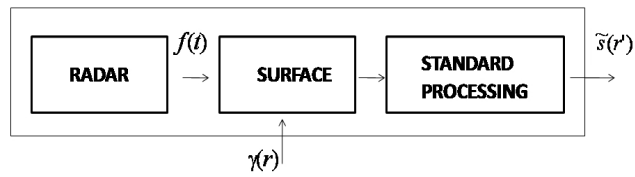


Figure 4.2: Global system.

Note that the phase term $-2k(r - z')$ plays a key role in the processing chain: it contains the two variables $r(x, y)$ and $z'(x, y)$, that describe the characteristics of the surface roughness at footprint and wavelength scales; these scales mainly influence the scattering phenomena and, consequently, the shape of the received waveform. The overall echo model expressed by Eq. (4.6) is the result of a mixed time-frequency approach that makes it possible to evaluate the altimeter echo as a function of the delay time, accounting for the roughness of the surface. This is obtained by using the frequency-domain backscattering coefficient computation presented in the Sect. 4.4, where it is clearly shown how the whole footprint contributes to modify the echo shape and width. The effect of the different scales on the altimeter return is detailed, which is a new result that sheds light on the processed data. We believe that this is the first step in developing an innovative rigorous systematic procedure to retrieve surface topographic properties by the analyses of altimeter data.

4.4 Electromagnetic Scattering

The scattering procedure adopted for computation of the reflectivity function in Eq. (4.6) is now briefly described.

A *facet model* of the scene is here considered for the electromagnetic scattering computation. This means that the scattered field is computed on regions (facets) of the surface much greater than the electromagnetic wavelength. It is worth noting that the meaning of the footprint and wavelength scales (see previous Sect. 4.2) can be here specified with respect to the roughness entering into the scattering problem: the macroscopic height represents the height $z(x, y)$ of the mean plane of the rough facet, while the microscopic height $z'(x, y)$ represents the roughness at wavelength scale relevant to the facet mean plane.

This means, in particular, that the facets orientation and distribution may

follow the fractal model fBm. Sample realization of this process are obtained by using the predictable process given by the WM function [9], thanks to its equivalence to the fBm process under certain constraints [9].

Each point of the WM function, in fact, represents the center of the rough facet from which the scattering contribution can be analytically computed [9]. In this way it is possible to superpose the returns from each facet (that is fractal at microscopic scale and at same time represents the elementary part of a band-limited fractal at macroscopic scale) by appropriately delaying the scattering contributions of the rough facets that compose the overall surface represented by the WM function.

A beam-limited altimeter with a narrow beam is considered. The information content of this work is not strictly dependent on the operating condition of the altimeter, and main results we derived can be easily applied to both conditions. The main difference of a pulse-limited altimeter with respect to a beam-limited one, in fact, is that some attention must be paid in limiting the portion of the illuminated surface contributing to the radar simulated echoes. The configuration here adopted is a beam-limited configuration, that is coherent, as mentioned in the Introduction of this Thesis, with the Cassini altimeter operating condition at low flights (the Cassini antenna is a very directive antenna; it has a beam-width of 0.006rad) so that the incidence angle can be taken as being small: let us also assume that the *small slope approximation* within the *physical optics solution* can be adopted to compute the scattered field. In this case, for any incident plane wave the backscattering co-polarized normalized cross section for a persistent fBm ($1/2 \leq H \leq 1$) to be used in Eq. (4.6), is computed as [9], see Fig. 4.3:

$$\sigma_{pp}^o = \frac{|R_p(\theta)|^2 k^2 T^2 (\cos \theta)^2}{H} \sum_{n=0}^{\infty} \frac{(-1)^n}{(n!)^2} \Gamma\left(\frac{(n+1)}{H}\right) \frac{(kT \sin \theta)^{2n}}{(\sqrt{2} kT \cos \theta)^{\frac{2n+2}{H}}}, \quad (4.7)$$

wherein:

- $R_p(\theta)$ is the Fresnel reflection coefficient of the mean plane for the p-polarized plane wave;
- k is the wavenumber;
- θ is the incidence angle (on the facet plane);
- $\Gamma(\cdot)$ is the Gamma function.

- T and H are the fractal parameters previously defined for the fBm process, see Eq. (3.1).

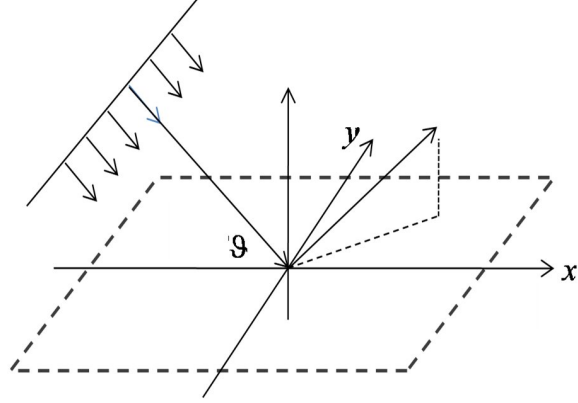


Figure 4.3: Geometry of the scattering problem.

The reflectivity function $\gamma(x, y)$ appearing in Eq. (4.6) represents the scattering properties of the surface, i.e. it provides the scattering amplitude from the facets that compose the entire surface of interest; it is obviously linked to the facet backscattering coefficient. The following expression for γ is here assumed, thus considering it a real function:

$$\gamma(x, y) = \sqrt{\sigma_{pp}^o(x, y)}. \quad (4.8)$$

The phase term, necessary to account for the different time shifting of the different face returns, is given by the $\exp(\cdot)$ term of Eq. (4.6). This term is made by two contributions: the first one due to the facet center distance to the sensor, and the second one, consisting of a uniformly distributed random phase, simulating the speckle effect.

It is important to highlight that the dimensions of the facets are set so that the range distance between the middle-points of neighboring facets is greater than or equal to the range resolution Δr of the radar. This constraint is set to assure that the surface discretization (performed in the coordinate system) is compliant with the need to correctly sample in time domain sampling of the received altimeter radar echoes, thus accomplishing the ground-to-slant range mapping. In this way the computation complexity is as much as possible reduced.

Chapter 5

Numerical Results

In this Section the analysis of the altimeter returns from a number of different surfaces is performed. In particular, the echoes from both canonical and fractal cases are computed. The main reason for considering some canonical cases of classical surfaces is to provide quantitative evidence that the presented model responds as can be expected by employing intuitive qualitative considerations, to present quantitative evaluations if more received echoes are somehow averaged, and to provide sense to the inversion procedure. Moreover, this approach allows also estimating the sensor sensibility to the scene variability.

The rationale of the proposed simulation procedure is showed in the flow-chart of Fig. 5.1: the first step is the surface generation. In order to see how the altimeter echoes change according to the different kind of scattering surfaces, the altimeter return is computed under the assumption of both fractal and non-fractal models: flat, tilted, layered, sinusoidal and fractal surfaces are considered at footprint scale; a subsection is dedicated to every mentioned scenario. But for the first example, any surface is assumed rough at wavelength scale. This large number of analysed cases is useful to highlight the relationship between the altimeter echoes and the ground scenario.

The surface is generated by means of ad hoc procedures for canonical scenarios and by means of Eq. (3.8) for fractal scenes; it is, obviously, discretized, each surface point representing the middle point of the facet described in Chapter 4 for the backscattering computation. The sizes of the represented scenarios range from about $30 \times 30 \text{ km}^2$ to $60 \times 60 \text{ km}^2$; as a consequence, the number of the scatterers, whose dimensions are set as described in Sect. 4.4, spans from 22500 to 9000000. The number of scatterers, whose dimensions are set as de-

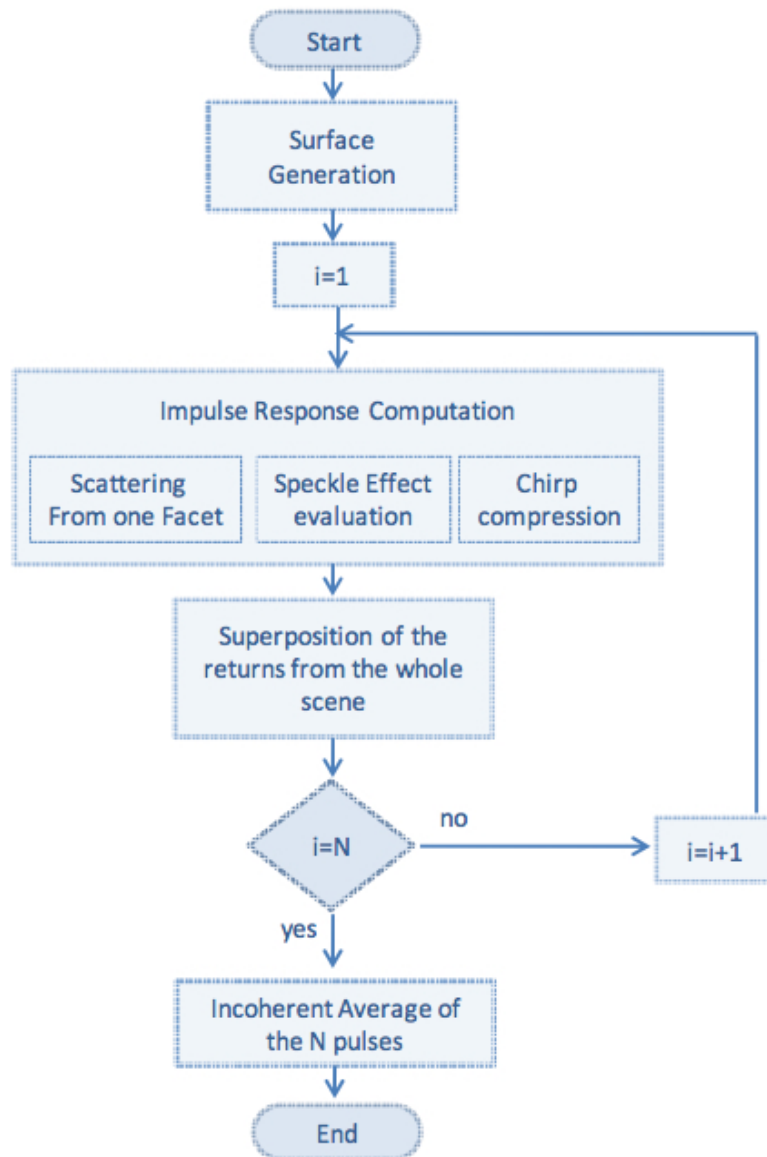


Figure 5.1: Logical scheme of the simulation procedure.

scribed in Chapter 4, spans from 22500 to 9000000. The number of scatterers is therefore very large, thus having a great number of returns mapped to the same range-bins. For this reason we experience a little speckle effect.

The subsequent logical step is to compute the signal received by the altimeter when it transmits toward the previously generated surface one chirped signal. This step is composed by two blocks: the first one computes the impulse response of the system in Fig. 4.2; in fact, the signal that the altimeter would receive by a single scatterer of the surface is computed. To this aim three operations are needed: the single facet scattering computation (Eq. (4.7)), the speckle effect evaluation and the chirp compression. The second block realizes the superposition of the computed returns from all the scatterers present in the scene, thus providing the echo received by the altimeter as in Eq. (4.6). For every scenario, these two blocks produce two plots, the power impulse response of the system at nadir and the overall echo power respectively, on the same graph, in order to highlight the difference between the simulated signal received from the whole scene and the signal that would be received from a single scatterer on the ground at the nadir direction. The (mean) power $P_{\text{rx}}(t)$ within a RF cycle is computed as:

$$P_{\text{rx}}(t) = \frac{1}{2} |\tilde{s}(t)|^2, \quad (5.1)$$

and this value is normalized to the peak value of each graph.

These computations are repeated until the desired number of pulses, N , is collected from the same synthesized scenario.

Finally, an incoherent average of the N -burst is performed. In the presented simulations the speckle effect is reduced by incoherently averaging 15 echoes (1 burst) from the same scenario. For each simulation three graphs are in fact generated:

- the power received by the altimeter versus for a single pulse;
- the power (incoherently) averaged on a burst of data composed of fifteen pulses (this value is chosen with reference to the Cassini altimeter, which will be considered in the following);
- the power (incoherently) averaged on an infinite number of pulses (this limiting value to be considered as ideal choice to suppress any speckle effect in an ideal altimeter).

As above mentioned, in every plot the received power pulse, sampled at the rate reported in Table 5.1, is shown, and the system impulse response, see

Fig.4.2, is also depicted. The values of the parameters used in the simulated canonical cases are given in Tables 5.2 and 5.3. The computation times range from about 10 sec to 200 sec, according to the scenario size, on a dual core intel processor at 2,2 GHz, with 2 gigabytes of RAM memory.

Antenna beam-width	0.35°
Carrier wavelength, λ	2cm
Platform altitude, h	5000km
Antenna footprint, S	30 km
Return sampling rate, Δr	35m

Table 5.1: ALTIMETER SYSTEM PARAMETERS

TILTED SURFACE	
Slope, α	1.8°
SINUSOIDAL SURFACE	
Amplitude, A	100m
Spatial period, λ_s	3000m
LAYERED SURFACE	
Thickness, d , Fig. 5.5	100m
Thickness, d , Fig. 5.6	100m
First layer relative electric permittivity, ϵ_r	4
First layer conductivity, σ	10^7 S/m

Table 5.2: SURFACE GEOMETRICAL PARAMETERS

5.1 Planar Surface

In Fig. 5.2(a) the simplest case is shown, i.e., a sphere of radius with no topography. In this case only a limited area on the surface around the stationary phase points contributes to the received signal; the diameter is, using the values of Table I, approximately reduced to 450 m. As expected, the modulus of the received signal (diamonds) is coincident with the modulus of the impulse response (dotted line). In Fig. 5.2(b) the case of a flat surface at footprint scale, with rough microscopic behaviour, is shown: in this case, the whole footprint

WM SURFACE	
Hurst coefficient, H	0.6
Overall scaling factor, B ; Figs. 5.7, 5.9,5.10	500m
Overall scaling factor, B ; Figs. 5.8,5.11	250m
Spectral separation, ν	e
Spatial period parameter, λ_0	30km
EQUIVALENT fBm SURFACE	
Fractal parameter, s ; Figs. 5.7, 5.9,5.10	$0.654\text{m}^{0.4}$
Fractal parameter, s ; Figs. 5.8,5.11	$0.327\text{m}^{0.4}$

Table 5.3: FRACTAL SURFACE

over the ground contributes to the received signal, thus slightly increasing the echo duration. This is more visible in Fig. 5.2(c), wherein the average received signal is reported.

5.2 Tilted Surface

Fig. 5.3 shows the altimeter return from a tilted surface at footprint scale, rough at wavelength scale. In this case, the variable r in Eq. (4.6) is given by:

$$r = \sqrt{(h' - x \tan \alpha)^2 + x^2 + y^2}. \quad (5.2)$$

The temporal width of the received signal increases significantly compared to the no slope case (Figs. 5.2). In particular, the width increase is strictly related to the maximum height excursion present in the footprint: the difference between the highest and the lowest point of the footprint is about 1100 m, consistent with the pulse spreading around its mean value. This result is clearer in Fig. 5.3(c), where the speckle effect is absent due to the average made over an infinite number of echoes.

It is worth noting that the off-nadir antenna pointing is equivalent to the surface tilting, for sufficiently slow off-nadir variations (except for the fact that off-nadir pointing directs the highest part of the antenna gain to a different range). Accordingly, its relevance and effect on the received pulse shape can be studied by following the same rationale presented in this section.

5.3 Sinusoidal Surface

In Fig. 5.4 the case of a sinusoidal surface at footprint scale, rough at the wavelength scale, is considered. In this case the variable r in the Eq. (4.6) is given by:

$$r = \sqrt{(h' - A \cos k_0 x)^2 + x^2 + y^2}. \quad (5.3)$$

In all the three graphs two peaks appear, corresponding to max and minimum heights of the topography. This is more clearly shown in the last figure, due to the average over an infinite number of pulses.

5.4 Layered Surface

The presence of possible canonical sub-layers is also analyzed: a sketch of the geometry is depicted in Fig. 5.5(a).

The results of the analysis are shown in Figs. 5.5-5.6. In these simulations the interfaces are both flat at footprint scale; the upper interface is rough at wavelength scale, whereas the lower is not. Accordingly, the echo is simulated by using the following formula.

$$\begin{aligned} \tilde{s}(r') \cong & \int_S p(r' - 2r) \exp[-2jk(r - z')] \gamma_1(r) dr + \\ & + \int p(r' - 2r - 2d\sqrt{\epsilon_r}) \left\{ \exp[-2jk(r - z) - 2jk_1(d + z - z_1)] \right. \\ & \cdot \left. \left((1 - R_1^2) R_2 \exp(-2jk_1 d) \frac{1 - (-R_1 R_2 \exp(-2jk_1 d))^N}{1 + R_1 R_2 \exp(-2jk_1 d)} \right) \right\} dr. \end{aligned} \quad (5.4)$$

where N is the number of bounces that contributes to a single range-bin, $R_{1,2}$ are the Fresnel coefficients of the first and second interface respectively, d is the thickness of the layer, and:

$$r = \sqrt{(h'^2 + x^2 + y^2)}. \quad (5.5)$$

The two examples assume a perfectly conducting half-space at the bottom so that $R_2 = -1$. Two peaks appear, corresponding to the two interfaces. By visual inspection of Figs. 5.5 and 5.6, obtained for different values of the layer thickness, it follows that the separation between peaks in the echo is equal to the optical thickness of the layer, $\sqrt{\epsilon_r}d$, about 170m and 85m in the first

and second example, respectively. It is also noted that the return is similar to that from sinusoidal topography, and this could cause some ambiguity in interpretation of the echoes.

5.5 Fractal Surface

In Figs. 5.7-5.9 the surface is modelled as fractal at both footprint and wavelength scale. The graph on top of each figure represents the surface profile used in the simulations of the altimeter return: its total length is equal to 30 km, coincident with the antenna footprint on the ground. The fBm surface $Z(x, y)$ is implemented, as said before, by the WM function and Eq. (4.6) holds with

$$r = \sqrt{([h' - Z(x, y)]^2 + x^2 + y^2)} \quad (5.6)$$

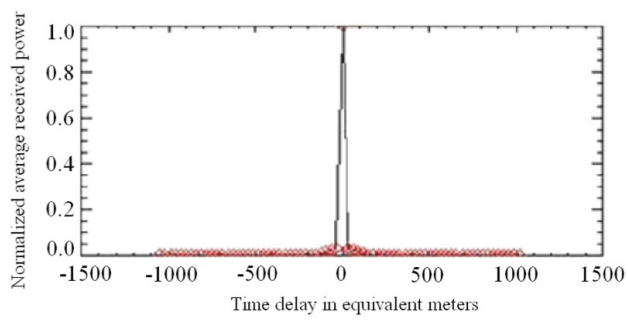
The surfaces in Figs. 5.7 and 5.8 have different values of the height scaling factor B: 500m for the first surface (Fig. 5.7) and 250m for the second one (Fig. 5.8).

For both cases the width of the received signal depends on the topography parameters. In particular, the higher value of B produces the wider received echo. As a matter of fact, the maximum height differences present in the footprints in Figs. 5.7 and 5.8 are approximately 400m and 250m, respectively, and coincide with the pulse widths. Note the link between the value of B and the surface height variations; more specifically, a reduction of 50% for the original value of B generates a corresponding reduction of the maximum height difference in the pulse of approximately 60% of its value.

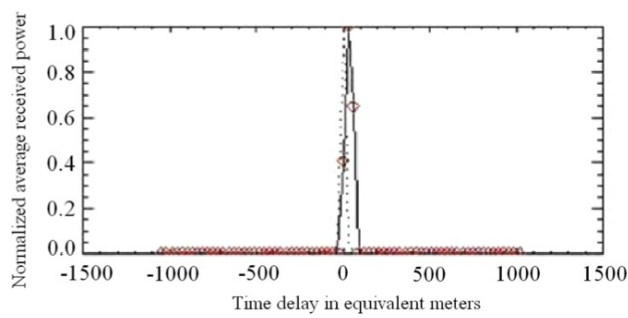
The shape of the pulse depends on the fractal parameters, too. In fact, whenever B increases the echo shape irregularities strongly increase as well. It is worth noting that the echoes in Fig. 5.7 show two peaks, around -100m and -300m; examination of the profile shows that most of its elevation level appears around these height values. This relation between the accumulation of the profile level around specific height values and the fractal parameters is an interesting point and deserves additional investigations. In Fig. 5.9 the same surface as in Fig. 11 is considered, but an off-nadir angle $\theta = 1.8^\circ$ has been included. The impressed off-nadir angle is equivalent to the slope of Fig.5.3. The echo width significantly increases as expected from the discussion in Sect.5.2.

The main difference between the echoes from the two profiles of Figs. 5.7 and 5.8 can be clearly seen in the last two figures, 5.10 and 5.11 where a

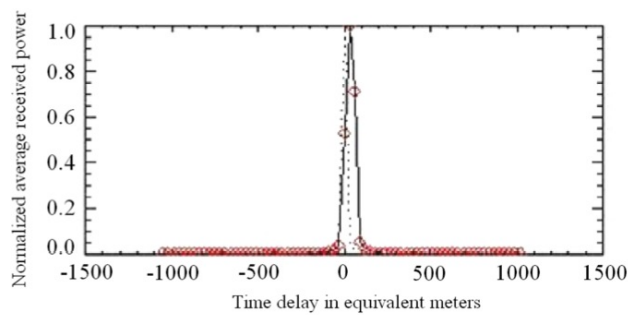
large collection of subsequent echoes (echograms) are displayed. The intensity of the echoes is grey-level coded; the adopted scale is depicted at the top of the pictures, being the maximum and minimum ranging from white to full black, respectively. The width of the received pulses is reported on the vertical axis and is measured in meters, while the distance to the spacecraft position is represented on the horizontal axis and is measured in kilometers. By visual inspection of these graphs it appears that the dispersion of the returns around the mean value in Fig. 5.10 is on the average greater than that of the Fig. 5.11. This is explained by observing that the larger B value in Fig. 5.10 affects the the profile along the vertical axis thus changing the topography at footprint scale and significantly modifying the altimeter return.



(a)

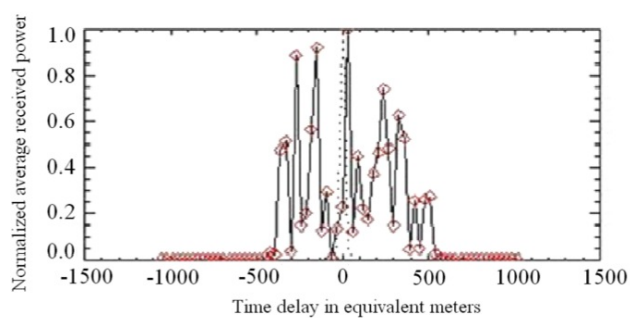


(b)

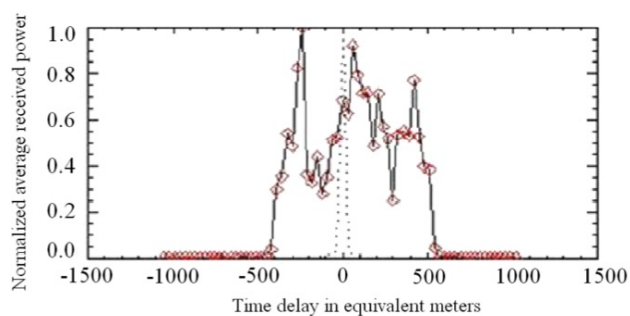


(c)

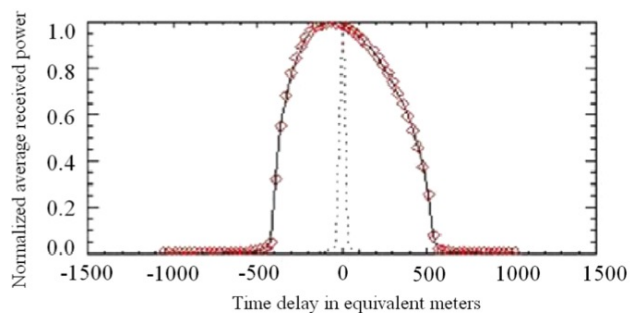
Figure 5.2: Simulated echo power, normalized to its peak value, from a surface: 5.2(a) flat at footprint scale, smooth at wavelength scale, 1 pulse; 5.2(b) flat at footprint scale, rough at wavelength scale, 1 pulse; 5.2(c) flat at footprint scale, rough at wavelength scale, average over 15 transmitted pulses. The echo power is represented by diamonds and its linear interpolation is represented by the solid line. The dotted line shows the impulse response of the system.



(a)

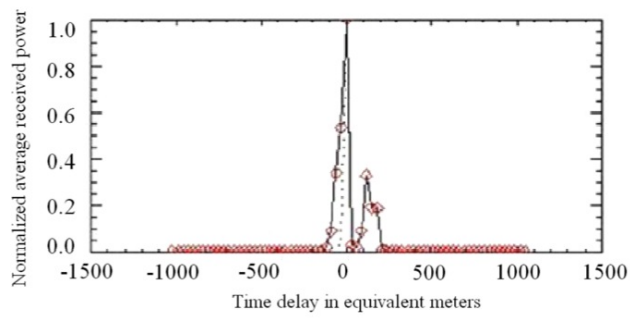


(b)

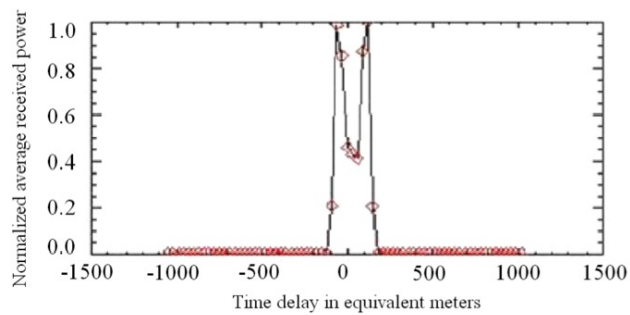


(c)

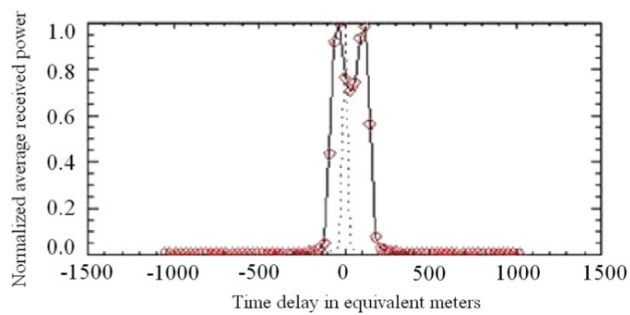
Figure 5.3: Simulated echo power, normalized to its peak value, from a surface tilted at footprint scale, rough at wavelength scale.: 5.3(a) 1 pulse; 5.3(b) average over 15 transmitted pulses; 5.3(c) average over an infinite number of transmitted pulses. The echo power is represented by diamonds and its linear interpolation is represented by the solid line. The dotted line shows the impulse response of the system.



(a)



(b)



(c)

Figure 5.4: Simulated echo power, normalized to its peak value, from a surface sinusoidal at footprint scale (amplitude = 100 m, wavelength = 3000 m) rough at wavelength scale: 5.4(a) 1 pulse; 5.4(b) average over 15 transmitted pulses; 5.4(c) average over an infinite number of transmitted pulses. The echo power is represented by diamonds and its linear interpolation is represented by the solid line. The dotted line shows the impulse response of the system.

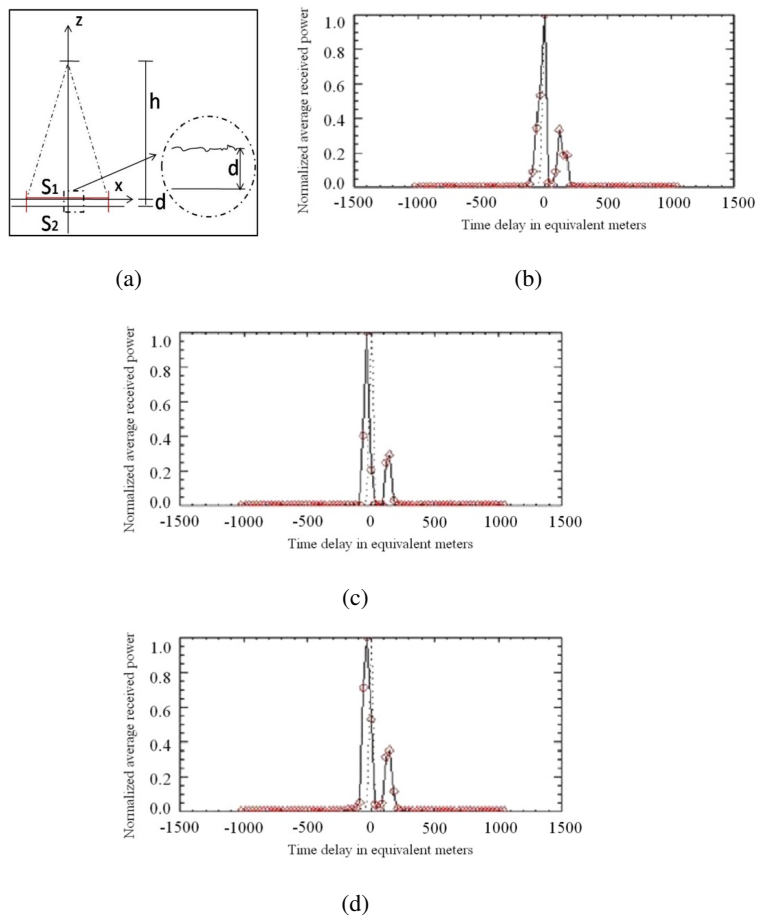


Figure 5.5: 5.5(a) Sketch of the layered geometry. The first layer is rough at wavelength scale, the second one is smooth. $\epsilon_r = 3$, $\sigma = 10^{-7} S/m$. In the subsequent subfigures the received power echo, normalized to its peak value. The layer thickness is $d = 100m$. 5.5(b) 1 pulse; 5.5(c) average over 15 transmitted pulses; 5.5(d) average over an infinite number of transmitted pulses. The echo power is represented by diamonds and its linear interpolation is represented by the solid line. The dotted line shows the impulse response of the system.

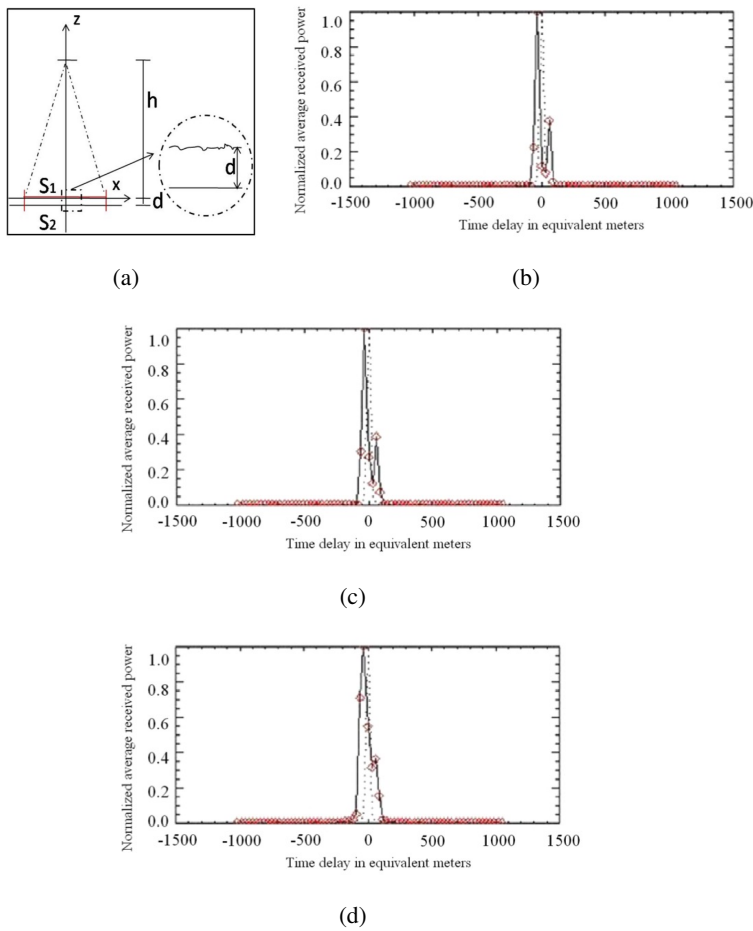


Figure 5.6: 5.6(a) Sketch of the layered geometry. The first layer is rough at wavelength scale, the second one is smooth. $\epsilon_r = 3$, $\sigma = 10^{-7} S/m$. In the subsequent subfigures the received power echo, normalized to its peak value. The layer thickness is $d = 50m$. 5.6(b) 1 pulse; 5.6(c) average over 15 transmitted pulses; 5.6(d) average over an infinite number of transmitted pulses. The echo power is represented by diamonds and its linear interpolation is represented by the solid line. The dotted line shows the impulse response of the system.

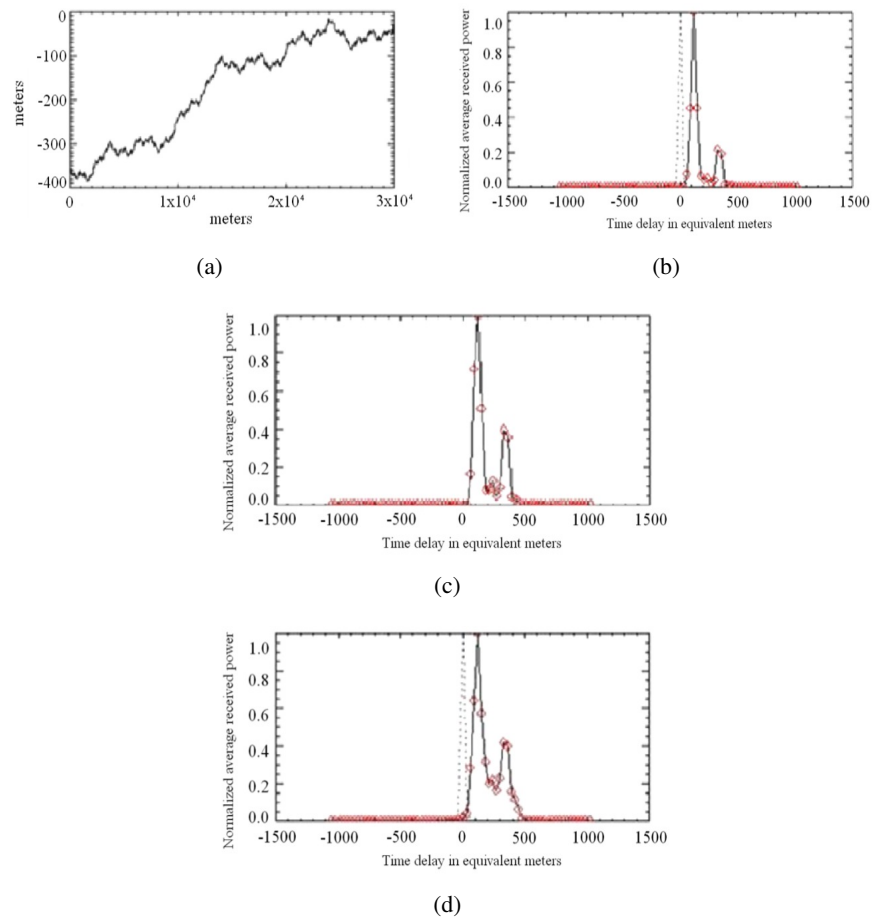


Figure 5.7: Received power echo, normalized to its peak value, from a fractal surface 5.7(a) at both footprint and wavelength scale ($H = 0.6$, $B = 500m$); 5.7(b) 1 pulse; 5.7(c) average over 15 transmitted pulses; 5.7(d) average over an infinite number of transmitted pulses. The echo power is represented by diamonds and its linear interpolation is represented by the solid line. The dotted line shows the impulse response of the system.

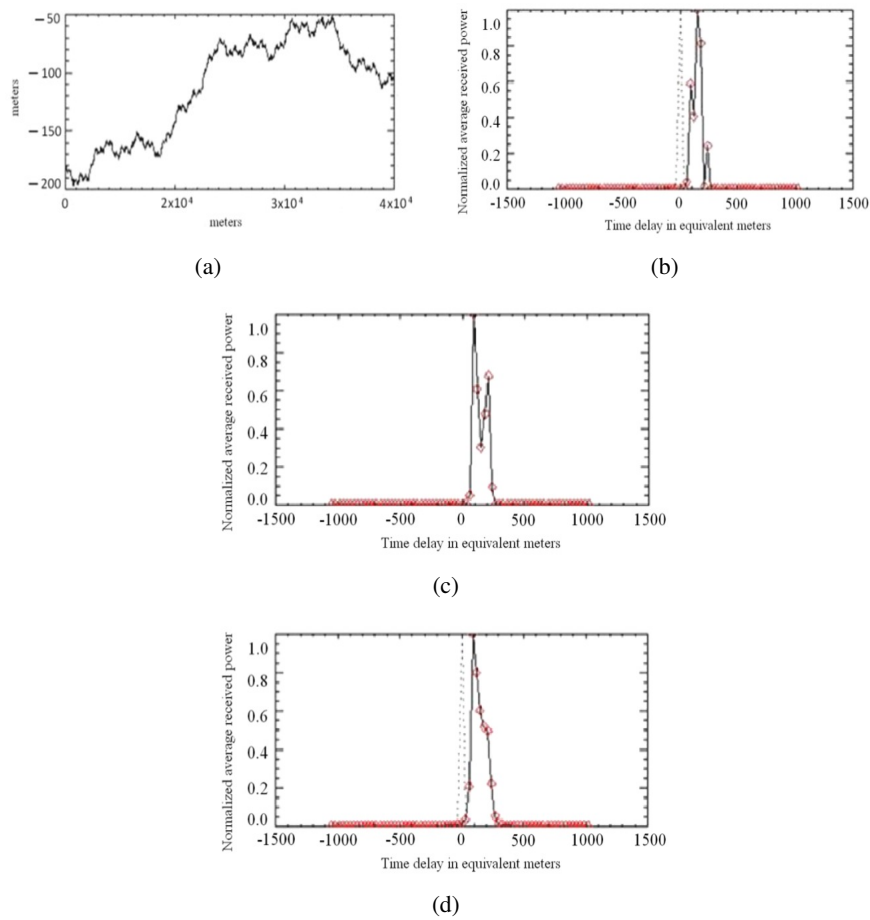


Figure 5.8: Received power echo, normalized to its peak value, from a fractal surface 5.8(a) at both footprint and wavelength scale ($H = 0.6, B = 250m$); 5.8(b) 1 pulse; 5.8(c) average over 15 transmitted pulses; 5.8(d) average over an infinite number of transmitted pulses. The echo power is represented by diamonds and its linear interpolation is represented by the solid line. The dotted line shows the impulse response of the system.

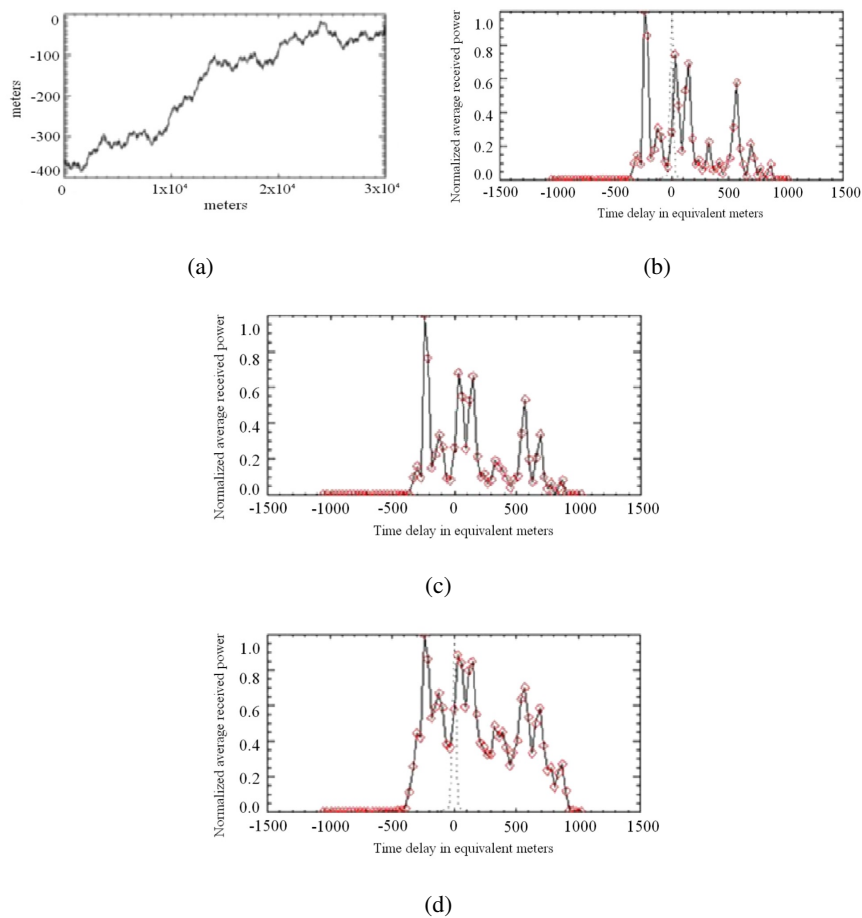
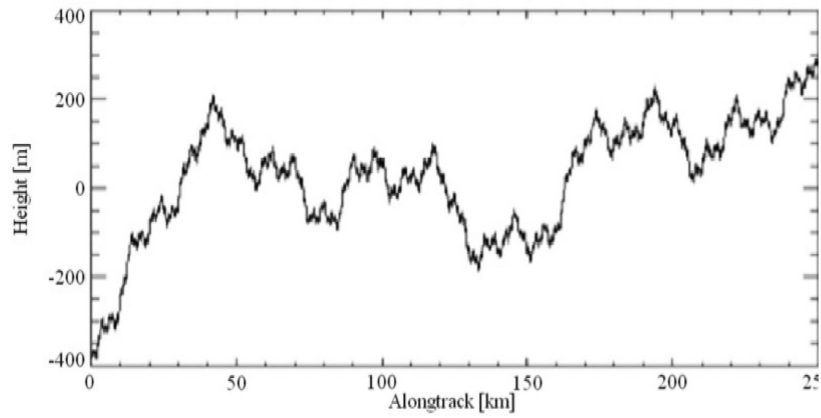
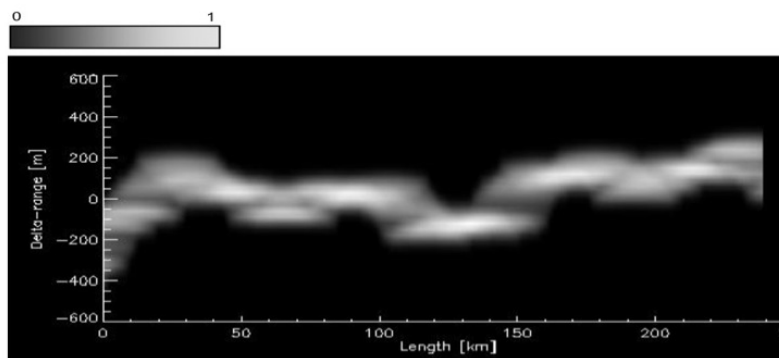


Figure 5.9: Received power echo, normalized to its peak value, from a fractal surface 5.9(a) at both footprint and wavelength scale ($H=0.6$, $B=500\text{m}$, same as Fig. 5.7) with off-nadir pointing of 1.8 deg (like slope in Fig. 5.3; 5.9(b) 1 pulse; 5.9(c) average over 15 transmitted pulses; 5.9(d) average over an infinite number of transmitted pulses. The echo power is represented by diamonds and its linear interpolation is represented by the solid line. The dotted line shows the impulse response of the system.

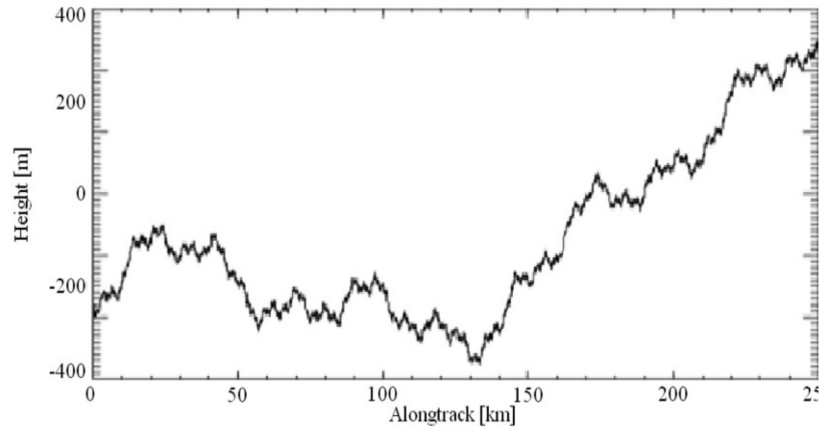


(a)

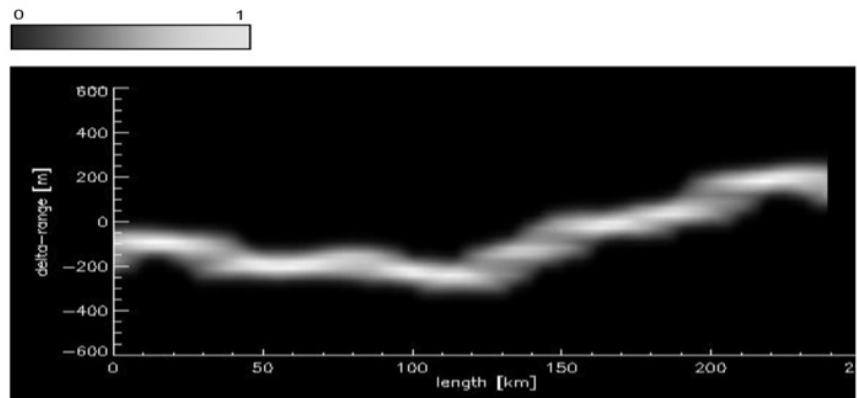


(b)

Figure 5.10: 5.10(a) WM surface profile with $H=0.6$, $B=500\text{m}$; 5.10(b) Corresponding echogram by using the simulated return pulses.



(a)



(b)

Figure 5.11: 5.11(a) WM surface profile with $H=0.6$, $B=250\text{m}$; 5.11(b) Corresponding echogram by using the simulated return pulses.

Chapter 6

Experimental validation

In this Chapter the previously presented simulation procedure has been applied to the data collected by the Cassini-Huygens spacecraft (see Chapt. 1). In fact the proposed study has been developed starting from the need of the JPL (NASA) to correctly understand the echoes received by the Cassini altimeter from Titan's surface. This is because many received pulses have an irregular shape that cannot be explained by the Brown's models, therefore it is very interesting trying to understand the phenomena that determine the pulse shape affecting the shapes of the pulses. The Chapter presents two sections: the first one describes the radar system of Cassini Huygens; the second one shows the results of the application of the proposed model to the Cassini data.

6.1 Cassini Mission Radar Altimeter

As before said, one of the main objectives of the Cassini Radar Mission is Titan coverage [49]. In order to study the surface properties and processes of Titan, the spacecraft has made a number of close flybys during its four year nominal mission (extended to 2017). During these flybys, the Cassini Radar and other instruments onboard the spacecraft has conducted intense observations, in order to achieve the scientific goals. The first targeted fly-by of Titan (Ta) occurred on Tuesday, October 26, 2004 at 15 : 30 UTC [50]. While operating as an altimeter (ALT mode), the instrument will be able to measure surface elevations along the sub-satellite ground tracks. At an inhospitable temperature (around 90 K), the chemistry that drives surface processes is fundamentally different from Earth's: it is methane to perform many of the same functions on Titan that water does on Earth. As a consequence, the mapping of Titan

is an especially challenging puzzle, because the most likely constituent materials in this chemical and temperature regime are likely to exhibit different scattering properties than at Earth and Venus, the only other worlds mapped by spaceborne radars [51]. In the frame of the Cassini Radar Program, the Cassini Processing of Altimetric Data (PAD) System has been conceived in order to process the data collected by the Cassini Radar, while operating as an Altimeter. The integrated software application offers all the specific instruments needed to process, manage, visualize, archive and disseminate the scientific products containing all the retrieved information about the Titan surface topography, starting from the raw data as provided by JPL/NASA. The height retrieval functionality, core of the altimetric processing, is performed by using implemented algorithms which are based on ad hoc developed mathematical techniques necessary to simulate analytically the average return power waveform, as obtained from the received signal, in order to cope with the particular operating conditions, and with the expected occurrence of off-nadir measurements. In the following, after a brief introduction concerning the Cassini Radar, an overview of the PAD System architecture in terms of implemented Radar Altimeter General Waveform Model and Its Application to Cassini Mission functionalities, component applications and system design will be given.

6.1.1 The Cassini Radar

The Cassini Radar is a multimode microwave instrument that uses the 4 m high gain antenna (HGA) onboard the Cassini orbiter. The instrument operates at Ku-band (13.78 GHz or 2.2 cm wavelength) and it is designed to operate in four observational modes (Imaging, Altimetry, Backscatter and Radiometry) at spacecraft altitude below 100000 Km, on both inbound and outbound tracks of each hyperbolic Titan flyby, and to operate over a wide range of geometries and conditions [51]. The instrument has been designed to have a wide range of capabilities in order to encompass a variety of possible surface properties. From signal to noise and data rate considerations, the ALT mode is planned to operate at S/C altitudes between 4000 and 9000 Km, approximately from 16 min before the closest Titan approach of each Titan flyby until 16 min after the closest encounter. During such operation, the radar uses the central, nadir-pointing antenna beam (Beam 3, a circular beam 0.350° across) for transmission and reception of chirp pulse signals at a system bandwidth of 4.25 MHz [51],[52]. The Altimeter operates on “burst mode”, similar to the imaging mode. When the ALT mode is executed, bursts of frequency modulated pulse signals (chirp pulses) of $150\mu s$ time duration and at 5 MHz bandwidth will be

transmitted in a Burst Period (the Burst Repetition Interval is 3333 ms). The transmit time varies from 1.4 to 1.8 μ s. The number of pulses transmitted in each burst will vary throughout a single flyby pass. The collected altimeter measurements are expected to have horizontal resolutions ranging between 24 and 27 Km, and a (final achievable) vertical resolution of about 30 m. In addition to the limitation due to the intrinsic vertical resolution, the accuracy in estimating the relative surface elevation (that is, the change in local surface elevation relative to a reference datum) depends also on the topographic relief of the surface as well as on the knowledge of the spacecraft's ephemeris and attitude. An estimate of such accuracy is between 100 and 150 m.

6.1.2 Cassini PAD System Overview

As part of the Cassini Radar Program, ASI required to process and exploit the Cassini altimetry data, by means of an ad hoc developed system: the Cassini Radar PAD. The implemented system contains the HW and SW tools necessary to:

- receive and elaborate the Cassini Radar Altimeter instrument raw,
- generate the science data products from the received Cassini Radar Altimeter data sets,
- archive and manage the science data products within the system.

The system is able to manage BODP files supplied by JPL. Basically, these are data sets at various stage of processing, organized as time-ordered records for each burst. They are fixed header length and fixed record length files, compliant to PDS standards. The header is an attached PDS label. According to SIS, BODP products come in three different record formats (see [53] and [54]):

- Short Burst Data Record (SBDR),
- Long Burst Data Record (LBDR),
- Altimeter Burst Data Record (ABDR).

The SBDR is produced for every Titan flyby, and it is divided into three consecutive segments from three different levels of processing (Engineering, Intermediate Level and Science Data Segments) containing radar telemetry,

timing and spacecraft geometry information and all relevant scientific data. The LBDR is simply a SDBR which also contains sampled echo data. The LBDR data for altimetry supplied by JPL to ASI will contain only basic engineering unit conversions and geometry calculations. The ABDR data is the same as the SBDR, except that it includes the altimeter profile. The ABDR file is generated from the altimeter processor and it can be furthermore used to perform additional altimetry processing. The physical architecture of the PAD System is composed by several software components distributed on two operating system platforms. The server platform, supported by a Linux operating system, hosts the local data archive and acts as the domain server, while the client platform, supported by a Windows® XP Professional operating system, hosts the data processing subsystem. On the server platform, the logical component of the local data archive is the distributed file system: the local archive is accessed as a network drive by the data processing subsystem. The server handles the definition and the authorizations of the domain's groups and users to access the distributed resources. On the client platform, the data processing subsystem is represented by the Cassini Radar PAD application, installed with same functionalities on each workstation. The core of the system is represented by processing algorithms and tools developed in a Matlab® environment. Each tool is provided with a user-friendly GUI, which allows users to exploit all implemented functionalities. The core tools are integrated into a framework, which is a standard Windows application written following the design specifications and guidelines of the official guidelines for user interface developers and designers.

PAD Components The PAD System actually can be divided into six main logical components, briefly described in the following:

PAD Framework The main functionality of the PAD Framework software is to give users a global vision of the status of all the operations that can be made on the BODP files within the Cassini Radar PAD. It provides easy access to all system functionalities. Users can select the flyby to operate and start any operation available for the processing of telemetry files.

PAD File Manager The PAD File Manager is the software component that allows users to import the PDS telemetry files into the Local Archive, and to deliver the output ABDR products to the scientific community. The LBDR data retrieval can be executed through the JPL secure HTTPS site, or from any file system location indicated by the user. The delivery functionality can publish the ABDR file on a public FTP repository and/or copy it to a writable portable transfer media.

PAD Data Publisher The PAD Data Publisher is the software component containing all the commands and the methods that allow users to forward the ABDR files to the Cassini Ground System repository located at JPL. The produced ABDR file is not physically sent nor moved to the Cassini Ground System repository located at JPL. Once the PAD File Manager has published the ABDR files to the public FTP repository, the scientific community receives an e-mail notification to access the password protected repository in order to download the new available file.

ABDR Production Tool The off-line ABDR Production Tool (PT) retrieves the input LBDR files by managing a list of LBDR files locally stored, allowing user to select the input file. After interactive selection of the LBDR file to be processed, the tool proposes to start the creation of subsets of the input LBDR product (intermediate PT Files) each containing only data records pertinent to one of the active Cassini Radar operational modes, i.e. Altimeter, SAR and Scatterometer mode. These files are created for internal use and stored into the local archive in both binary and ASCII format, in order to be accessed by SLT. The PT allows user to perform the generation of the ABDR product starting from the selected LBDR file. Moreover, user is allowed to interactively modify selected keywords into ABDR PDS label. An ABDR file is produced which contains records for only the two periods (one inbound, one outbound) in which the radar is in altimeter mode, by filling in automatically all the appropriate data fields in the Science Data Segment with the values obtained from SLT processing, and by filling the end of each record in the LBDR file with the values resulting from range compression of sampled echoes data counts (i.e. the altimeter profile), starting from SLT results files. When LBDR processing is terminated, the ABDR PT stores the new file into the local archive along with a report file. Data contained into the ABDR product shall be validated by using SLT functionalities, before submission to the local file server.

Science Look Tool The off-line Science Look Tool (SLT) is in charge to perform the altimetric processing implementing echo models based on the Brown's model introduced in Chapt. 2. It is a graphical application including procedures and algorithms designed to check and simulate the performances of the Cassini Radar Altimeter through calculation, visualization and plotting of relevant parameters. The SLT uses an intermediate BODP file produced by the ABDR Production Tool, stored into the local archive, and it automatically performs range compression of sampled data. The SLT evaluates the altimeter profile range start, altimeter profile range step and altimeter profile length required for the PT ABDR production functionality, starting from compressed

data. Each compressed burst is constituted of N_p chirp pulses. In order to reduce the speckle, a single pulse is obtained by averaging all the received pulses within the burst. Hence, each compressed burst becomes an array containing only one averaged pulse compressed echo. The averaged bursts are stored into internal memory as two dimensional arrays. The range compressed data are used to perform waveform analysis and final altitudes estimate by using different altimetry models previously implemented. In addition, the tool permits user to simulate the performances of the Cassini Radar Altimeter, thus allowing obtaining a complete analysis of ALT data from a scientific perspective. In order to infer the significant geophysical parameters describing the surface's topography from the altimetry data, a Maximum Likelihood Estimator (MLE) has been implemented to be enclosed in the developed algorithm. The Maximum Likelihood Estimator algorithm is based on fitting averaged bursts with a theoretical model describing the Radar Impulse Response. The algorithm is able to select automatically which is the best theoretical model to be used during the processing. The selection is based on threshold criteria related to the current value of the off-nadir angle, in order to cope with the expected occurrence of near-nadir measurements along the hyperbolic trajectory followed during the flyby. All the performances have been numerically evaluated: this method ensures the best fitting of data, thus reducing the errors in heights estimation. The SLT Tool allows users to specify the default processing parameters by using a Configuration File containing:

- threshold values for off-nadir angles
- minimum number of MLE iterations
- first attempt values
- thresholds for MLE Error Reducing Procedure, etc.

The SLT provides several auxiliary functionalities that allow the user to obtain the complete monitoring of both processing and results. On user request, the SLT provides 2-D or multi-plots of S/C and Radar ancillary data, processing results and algorithm configuration. All the results can be exported (i.e. printed/saved) by user. In addition, on user request, a report file in xml format is generated containing all the results produced by the SLT, e.g. relevant processing parameters, MLE procedure results, relative elevations of Titan's surface vs. along-track distance (i.e. topographic profiles), altimeter waveforms vs. range bins, ancillary data (e.g. observation geometry and orbital

parameters vs. time, instrument data, etc.), surface parameters vs. along-track distance, etc. It will be used by scientists for further validation of data, which is propaedeutical to ABDR production.

Map Tool The off-line PAD Map Tool (MT) is a graphical application that allows users to visualize and navigate through Titan's 2D and 3D maps, finalized to the analysis of their informative content, as immediate instrument of interpretation of scientific data. From the point of view of scientific surveying, altimetric maps could be confronted and joined with maps obtained by radiometric surveys and with the analysis made by other instruments onboard the Cassini Spacecraft, in order to provide a global vision, as far as it is possible, of the characteristics of Titan's surface. The purpose of MT is the production of altimetric regional maps obtained by visualization of sub-satellite ground-tracks and overlapping of data collected along tracks to a pre-existent map of Titan, over the region illuminated by the Cassini Radar in high-resolution ALT mode, for each Titan fly-by. Hence, Titan's maps represent the final results of data processing. The realization of the altimetric map can be accomplished by referencing the radar altimetry profile with respect to the surface of Titan. The Titan's altimetric maps are generated starting from SBDR, LBDR and BIDR data files, and from output data produced by the SLT (e.g. the topographic profile with information about the surface slope, etc.) which could be superimposed to referenced images of Titan surface in a given projection. The content of SBDR, LBDR and BIDR data files is extracted by means of a Data Production Utility, which saves all relevant information needed to produce MT datasets (map internal files) containing satellite geometry, Scatterometer, Radiometer and SAR data, which becomes then available to Map Tool for visualization. The SLT output data needed to MT procedures execution are retrieved from the local archive or database. Titan's images (e.g. Mercator albedo maps from HST, ESO, etc, images acquired by optical observation by the Cassini ISS, etc.) to be used as map background, shall be made available, for example by the Cassini Ground System at JPL/NASA, and shall be also stored in the local database. All maps produced by the Map Tool are stored into the local archive, for further distribution.

6.2 The proposed model in the Cassini framework

In this Section the application of the model presented in the previous chapters is showed. In particular, the aim of this section is to put in evidence how the actual data collected by the spacecraft can reveal precious value-added

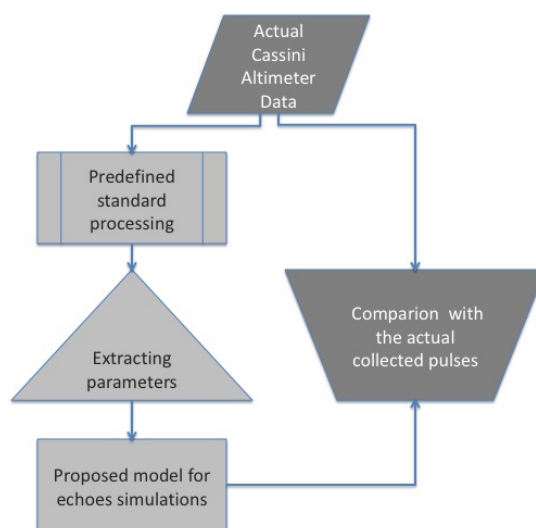


Figure 6.1: Sketch of the logical steps followed in the model validation on the Cassini altimeter data.

information about the unknown surfaces of Titan.

This objective is obtained by applying the procedure sketched in fig. 6.1.

The first step is to read, by means of the PAD system before mentioned, the collected and standard processed data. Then, the analysis of these data is made to the aim to achieve the information necessary to apply the presented simulation model. After having obtained the received simulated echoes, a comparison between simulation results and experimental data is performed and showed.

Two subsections follow, to explain the scenario information extraction and the results of the comparison, respectively.

6.2.1 Estimating fractal parameters

The considered set of data has been collected by the Cassini spacecraft during a flyby of Titan (T19). By considering the ABDR data relative to that passage, several parameters of the scenario under survey have been extracted, that enter in the proposed model.

- Geographical information, (Latitude and Longitude, of the passage);

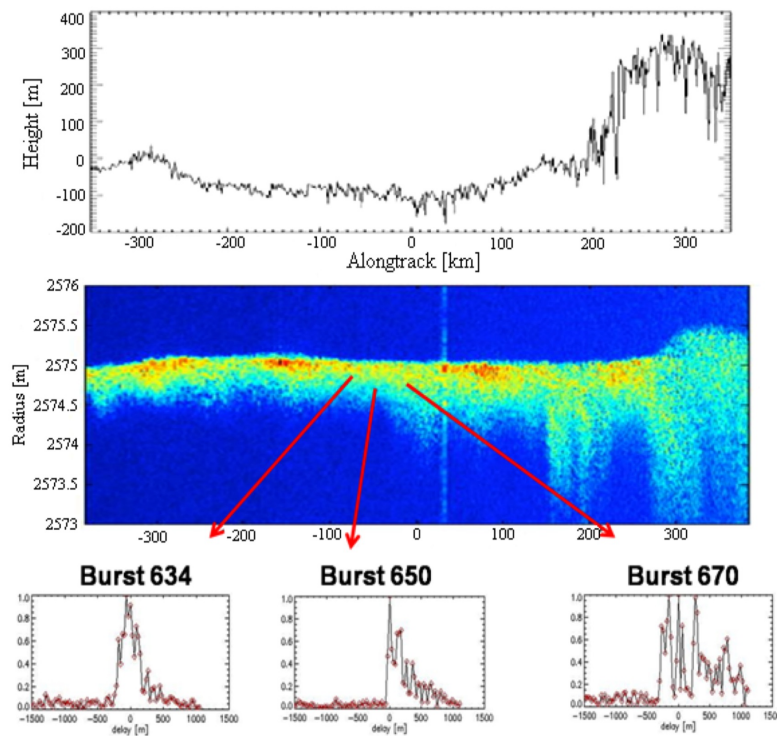


Figure 6.2: Flyby T19 detected profile with the relative echogram and three different received pulses (averaged on the relative bursts).

- inbound or outbound phase of flyby;
- Height of flight of the platform;
- Off-nadir angle;
- Height profile obtained by Threshold Detection algorithm.

In Fig.6.2 an echogram from the outbound segment of T19 is shown, together with the estimated profile (with the TD algorithm) and some received pulses collected in the central region of the flyby (bursts 634-650-670) [26] chosen for the comparison with the simulated data, reported in the subsequent pictures.

The analysis of the actual data makes it possible to evaluate the fractal parameters of the illuminated area following guidelines given in [12]. In particular, the fractal parameters (s, H) , which completely characterize the fBm process, are estimated by analyzing the height profile obtained by means of TD processing of the data collected by the spacecraft. This estimation procedure is matter of research: here we employ a variogram (see Chpater 3) based technique [9, 48, 12]: from previous chapters we know that

$$\begin{aligned} Q(l) &= \langle |z_m(x+l) - z_m(x)|^2 \rangle & (6.1) \\ &= \langle |z(x+l) - z(x)|^2 \rangle + 2\sigma_n^2 \\ &= Q_z(l) + 2\sigma_n^2, \end{aligned}$$

where $\langle \cdot \rangle$ stands for statistical mean, and $Q_z(l)$ is the structure function of the noiseless process; in 6.2 use has been made of statistical independence of z and n .

It is important to note that the above definition of the stucture function applies not only to wide-sense stationary stochastic processes, such as the classical ones; but also to non-stationary processes, provided that their increments are wide-sense stationary. The fBm model satisfies this last requirement, as detailed in Chapt. 3. For the fBm fractal model, we have (Chapt. 3):

$$Q_z(l) = s^2 l^{2H}, \quad (6.2)$$

$$Q(l) = s^2 l^{2H} + 2\sigma_n^2. \quad (6.3)$$

Therefore, it is possible to compute the “actual” structure function from the T19 TD height profile and to estimate the fractal parametrs (H, s) by fitting the data with the Eq. 6.3. Unfortunately, not always the fitting is successfull; some aspects of this procedure have to be improved. More precise techniques would be welcomed, and this is subject of future works.

6.2.2 Validation results

Once the fractal parameters have been, at least roughly, estimated, a two-dimensional surface with those parameters is generated [9], and the echoes scattered by this surface and received by the altimeter are simulated as indicated in Chapters. 4 and 5. The echoes obtained by the simulation runs can be finally compared with measured data.

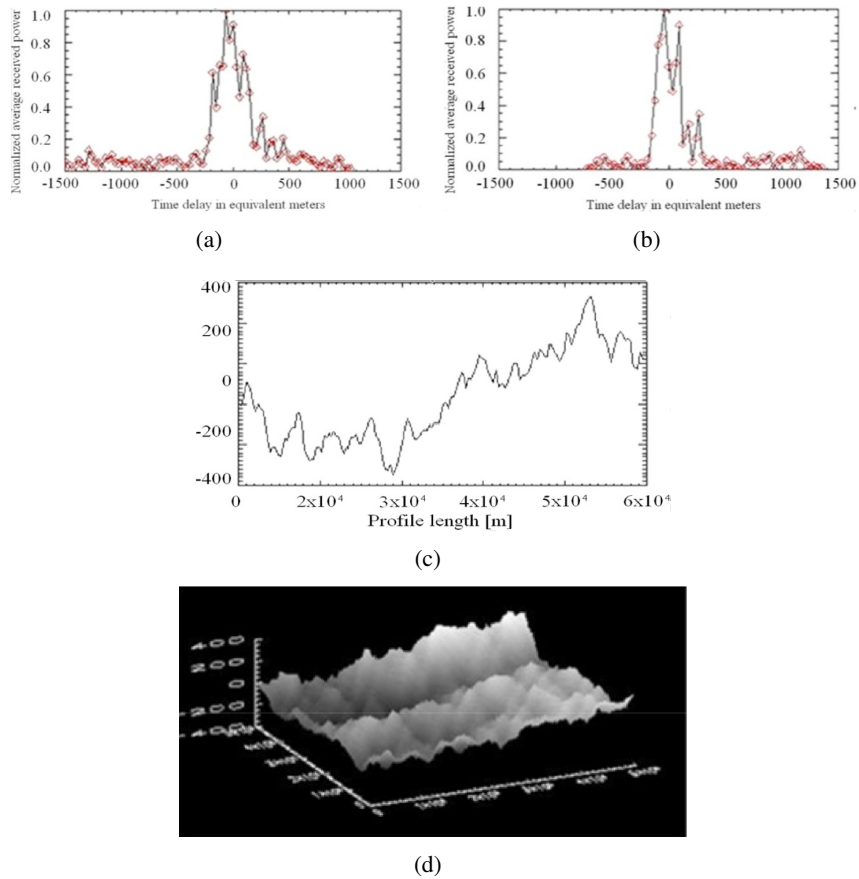


Figure 6.3: 6.3(a) Received pulse of the burst 634 of the T19 flyby Cassini mission; 6.3(b) simulated pulse. The values of the parameters estimated from the real data are: $H = 0.51$, $s^2 = 0,81$; 6.3(c) a cut of the simulated surface; 6.3(d) three-dimensional image of the simulated surface.

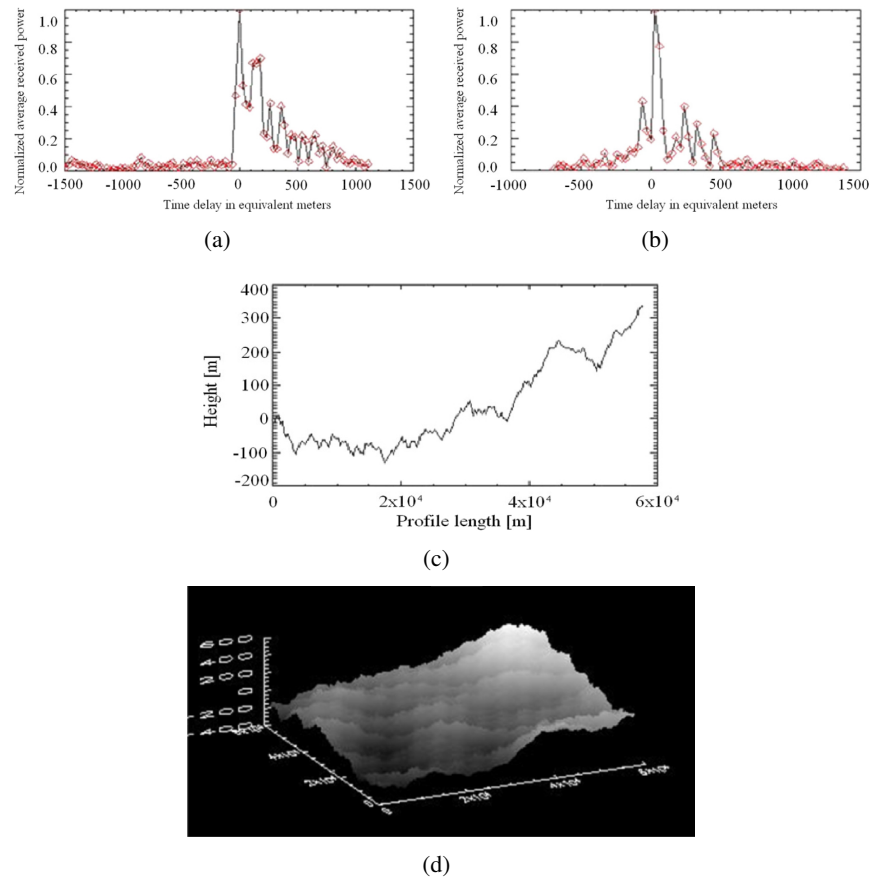


Figure 6.4: 6.4(a) Received pulse of the burst 650 of the T19 flyby Cassini mission; 6.4(b) simulated pulse. The values of the parameters estimated from the real data are: $H = 0.6$, $s^2 = 0,191$; 6.4(c) a cut of the simulated surface; 6.4(d) three-dimensional image of the simulated surface.

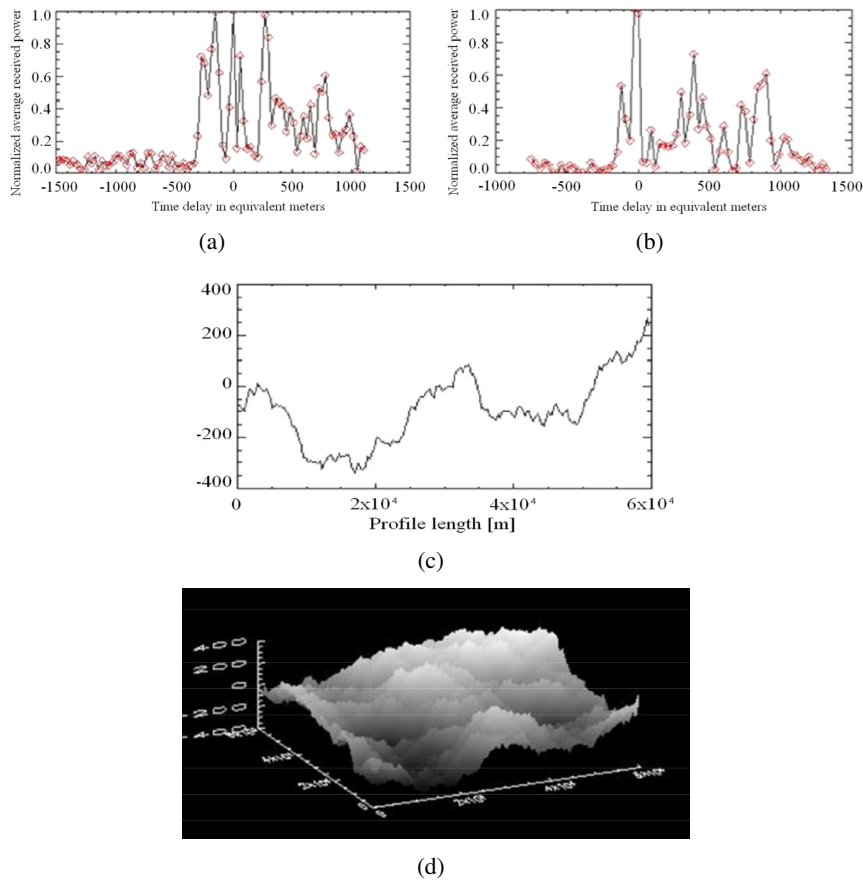


Figure 6.5: 6.5(a) Received pulse of the burst 670 of the T19 flyby Cassini mission; 6.5(b) simulated pulse. The values of the parameters estimated from the real data are: $H = 0.634$, $s^2 = 0,143$; 6.5(c) a cut of the simulated surface; 6.5(d) three-dimensional image of the simulated surface.

In Figs. 6.3, 6.4, 6.5, a direct comparison between some actual pulses and the corresponding simulated ones is made. As it is clearly seen by visual inspection of the figures, there is a remarkable correspondence between simulated and actual data. This strongly argues for a future in-depth examination of the previously analysed canonical cases, in order to plan a rigorous inversion procedure to retrieve the surface parameters, starting from the entire experimental data-set relevant to an actual mission.

Conclusions

In this dissertation a new model of the altimeter-received echoes, and its implementation in a simulation tool, have been described. Presently other simulation procedures exist, but these ones make use of models not so appropriate for land natural surfaces [5, 6, 7, 8, 9]. A logic scheme for the radar altimeter return computation totally based on fractal assumption has been implemented, because only the fractal geometry can efficiently represent the self-affinity properties of the natural surfaces. More specifically, we proposed a scale-dependent model of the surface, in order to appropriately understand and evaluate the effects of the different scales of observations on the radar altimeter return. We modeled the surface via an fBm (fractional Brownian motion) model, the best one to describe natural landscapes [5, 6, 7, 8, 9]. Since we are interested to describe the range of fractalness of the sensed surface involved in the altimeter acquisition, we appropriately defined the microscopic and macroscopic scales of observation. In details, surface portions (microscopic scales) contributing in single range bins have been described via the synthetic parameters of the regular stochastic fractal fBm [9] process. On the contrary, surface description at larger scales (macroscopic scales) has been accomplished by generating appropriate specific realizations of the sensed area obtained via a predictable stochastic fractal process, the WM function, whose parameters have been set in order to warrant the equivalence to the fBm process [9]. A rigorous procedure has been introduced to “superimpose” the fractal models to the mean planet curvature. A facet scattering model has been then adopted to evaluate the effects of both the microscopic and macroscopic scales contributions. The fractal PO (Physical Optics) approach [9], has been used, for the first time in radar altimetry modeling, to compute the single facet backscattering coefficient; then the superposition of the returns from the facets composing the whole surface has been performed in order to compute the altimeter echo.

The facet distribution and arrangement follow the fractal fBm law too; however, since we were interested to compute the received echoes, whose

shapes depends on the specific surface realization, we needed to deal with specific topographies, i.e. to generate fBm sample realizations. These ones have been obtained by using the predictable process given by the WM function [9], thanks to its equivalence to an fBm process under certain constraints [9]. These results have been applied to compute, in the time domain, the radar echoes by superposing the returns from each facet, i.e. by appropriately delaying the scattering contributions of the rough facets that compose the overall surface represented by the WM function. The novelty of the proposed procedure lies, first of all, in the improvement of the surface modeling and use of novel electromagnetic scattering evaluations. This has been obtained by adopting a fractal representation of the surface under survey, and through the usage of the appropriate scattering model for the echoes computation. It has been shown that this new model makes it possible to highlight the influence of the roughness of the surface (at different scales) on the scattering mechanisms and, as a consequence, on the echo shape and widths. An atlas of canonical situations can now be generated, in order to interpret the actual data collected by an altimeter. In this way not only a profile of the ground, but also (at least in principle) other topographic information, such as the roughness of the surface expressed in terms of fractal parameters as well as the presence of tilted planes, dunes, layers, etc., can be obtained. An experimental validation of this model has been conducted, by comparing the simulated data with samples of the actual ones collected by the Cassini spacecraft (a NASA-ESA-ASI joint mission) above Saturn's moon Titan. These preliminary but encouraging results suggest pursuing on the objective of implementing the proposed direct model in the altimeter processing chain, in order to obtain value-added information about the sensed surface. As a further step, implementation of an automatic inversion procedure to retrieve the fractal surface parameters from the actual data is in progress, along with the analytical solution of the superposition integral that represents the echo waveform, Eq. (4.6) A closed-form solution of this integral, even in asymptotic cases, should provide other methods to improve the above mentioned inversion procedure.

Bibliography

- [1] Brown, G. S., “The Average Impulse Response of a rough surface and its applications”, IEEE Trans. Antennas Propag., 25, 1977.
- [2] Berry, P.A.M. Freeman, J.A. Rogers, C. Benveniste, J., “Global Analysis of Envisat RA-2 Burst Mode Echo Sequences”, IEEE Trans. Geosci. Remote Sens., vol. 45, no. 9, pp. 2869-2874, Sept. 2007.
- [3] Montefredini, E., Morelli, F., Picardi, G., Seu, R., “A non-coherent surface backscattering model for radar observation of planetary bodies and its application to Cassini radar altimeter”, Planet. Space Sci, vol.43, no. 12, pp. 1567-1577, Mar. 1955.
- [4] Cassini-Huygens: Quick Facts. Saturn.jpl.nasa.gov. Retrieved 2011-08-20.
- [5] B.B. Mandelbrot, *The Fractal Geometry of Nature*. New York: Freeman, 1983.
- [6] B.B. Mandelbrot, *Gaussian self-affinity and fractals*, Springer, 2002.
- [7] K. Falconer, *Fractal Geometry*, Chichester, England: John Wiley & Sons, 1990.
- [8] J. Feder, *Fractals*, Plenum Press, 1988.
- [9] G. Franceschetti, and D. Riccio, *Scattering, Natural Surfaces and Fractals*, Academic Press, Burlington, (MA) USA, 2007.
- [10] M. K. Shepard, B. A. Campbell, M. H. Bulmer, T. G. Farr, L. R. Gaddis, and J. J. Plout (2001), “The roughness of natural terrain: a planetary and remote sensing perspective”, J. Geophys. Res., 106 (E12), 32777-32795.

-
- [11] D. L. Turcotte, "A fractal interpretation of topography and geoid spectra on the earth, moon, Venus and Mars", *Journal of Geophysical Research*, 92, E597-E601, 1987.
- [12] G. Franceschetti, P. S. Callahan, A. Iodice, D. Riccio and S. D. Wall, "Titan, Fractals, and Filtering of Cassini Altimeter Data", *IEEE Trans. Geosci. Remote Sens.*, vol. 44, no. 8, pp. 2055-2062, Aug. 2006.
- [13] Hayne, G. S., "Radar Altimeter Mean Return Waveforms from Near-Normal-Incidence Ocean surface scattering", *IEEE Trans. Antennas Propag.* AP-28, 687-692, 1980.
- [14] R.K. Moore and C.S. Williams, Jr., "Radar Terrain at Near Vertical Incidence", *Proc. IRE*, 45, 228-238, 1957.
- [15] J.K.Schindler, "Electromagnetic Scattering Phenomena Associated with Extended Surfaces", *IEEE internatl. Conv. Rec.*, 15-2, 136-149, 1967.
- [16] L.S.Miller and G.S.Hayne, "System study of the geodetic altimeter concept", final rept. On NASA contract No. NAS6-1829, Research Triangle Institute, 1971.
- [17] Bar, D. E. and Agnon, Y., "A fractal model for the sea state bias in radar altimetry", *Nonlin. Processes Geophys.*, 4, 213-222, doi:10.5194/npg-4-213-1997.
- [18] Agnon, Y., and M. Stiassnie (1991), "Remote Sensing of the Roughness of a Fractal Sea Surface", *J. Geophys. Res.*, 96(C7), 12,773-12,779.
- [19] Amarouche, L., P.Thibaut, J.P.Dumont, O.Z.Zanife, N.Steunou, and P.Vincent, 2004, *Marine Geo.*, 27, 1-2, pp, "Improving the Jason-1 ground retracking to better account for attitude effects".
- [20] Chelton D.B., J.C. Ries, B.J. Haines, L.L. Fu and P.S. Callahan, "Satellite altimetry", in "Satellite Altimetry and Earth Sciences", L.L. Fu and A. Cazenave (Eds), Academic Press, 2001.
- [21] Rodriguez, E., 1988, *J. Geophys Res*, 93, 14107, "Altimetry for Non-Gaussian Oceans: Height Biases and Estimation of Parameters".
- [22] Rodriguez, E., B. Chapman, 1989, *J. Geophys Res*, 94, 9761, "Extracting Ocean Surface Information from Altimeter Returns: The Deconvolution Method".

-
- [23] Rodriguez, E., J. Martin, 1994, *J. Geophys Res*, 99, 24971, "Assessment of TOPEX Altimeter Performance using Waveform Retracking".
- [24] J. Severini, C. Mailhes, P. Thibaut and J.-Y. Tourneret, "Bayesian estimation of altimeter echo parameters", *Proc. of IEEE International Geoscience & Remote Sensing Symposium (IGARSS'08)*, Boston, Massachusetts, USA, July 6-11, 2008.
- [25] Zebker H.A., Gim Y., Callahan P., Hensley S., Lorenz R. and Cassini Radar Team, "Analysis and interpretation of Cassini Titan radar altimeter echoes", *Icarus*, vol. 200, no. 1, pp. 240-255, Mar. 2009.
- [26] R.D. West, Y. Anderson, R. Boehmer, L. Borgarelli, P. Callahan, C. Elachi, Y. Gim, G. Hamilton, S. Hensley, M. A. Janssen, W.T.K. Johnson, K. Kelleher, R. Lorenz, S. Ostro, L. Roth, S. Shaffer, B. Stiles, S. Wall, L.C. Wye, H.A. Zebker", *Cassini RADAR Sequence Planning and Instrument Performance*", *IEEE Trans. Geosci., Remote Sens.*, vol. 47, no. 6, June 2009.
- [27] P. A. M. Berry, "Topography from land radar altimeter data: Possibilities and restrictions", *Physics and Chemistry of the Earth, Part A: Solid Earth and Geodesy*, Volume 25, Issue 1, 2000, Pages 81-88, ISSN 1464-1895.
- [28] Fedor, L.S.; Hayne, G.S.; Walsh, E.J.; , "Airborne pulse-limited radar altimeter return waveform characteristics over ice in the Beaufort Sea," *OCEANS '88. 'A Partnership of Marine Interests'*. Proceedings , vol., no., pp.1704-1710 vol.4, 31 Oct-2 Nov 1988 doi: 10.1109/OCEANS.1988.23815.
- [29] Fedor, L.S.; Hayne, G.S.; Walsh, E.J.; , "Ice-type Classifications From Airborne Pulse-limited Radar Altimeter Return Waveform Characteristics," *Geoscience and Remote Sensing Symposium, 1989. IGARSS'89. 12th Canadian Symposium on Remote Sensing., 1989 International* , vol.3, no., pp.1949-1952, 10-14 Jul 1989 doi: 10.1109/IGARSS.1989.576605.
- [30] Gómez-Enri, J.; Vignudelli, S.; Quartly, G.D.; Gommenginger, C.P.; Cipollini, P.; Challenor, P.G.; Benveniste, J.; , "Modeling Envisat RA-2 Waveforms in the Coastal Zone: Case Study of Calm Water Contamination," *Geoscience and Remote Sensing Letters, IEEE* , vol.7, no.3, pp.474- 478, July 2010 doi: 10.1109/LGRS.2009.2039193.

-
- [31] Papa F., Legresy B., Mognard N. M., Josberger E.G. and Remy F., 2002. "Estimating terrestrial snow depth with the Topex-Poseidon Altimeter and Radiometer". *IEEE Trans. Geosci. Remote Sensing*, 40 (10): 2162-2169.
- [32] R. K. Raney, "The Delay/Doppler radar altimeter", *IEEE Trans. Geosci. Remote Sens.*, vol. 36, no.5, pp. 1578-1588, Sept. 1988.
- [33] Martin-Puig, C. Ruffini, G. Marquez, J. Cotton, D. Srokosz, M. Challenor, P. Raney, K. Benveniste, J., "Theoretical Model of SAR Altimeter over Water Surfaces", *IEEE Geosci. Remote sens. Symp., IGARSS 2008*, vol. 3, pp. 242-245, Boston, 7-11 July 2008.
- [34] F. Rémy and S. Parouty, "Antarctic Ice Sheet and Radar Altimetry: A Review", *Remote Sensing*, Vol. 1, No. 4., pp. 1212-1239, December 2009.
- [35] Wingham, D. J., "A method for determining the average height of a large topographic ice sheet from observations of the echo received by a satellite altimeter", *Journal of Glaciology*, vol.41, Issue 137, pp.125-141, 1995.
- [36] R. J. Arthern, D. J. Wingham, and A. L. Ridout, "Controls on ERS altimeter measurements over ice sheets: Footprint-scale topography, backscatter fluctuations, and the dependence of microwave penetration depth on satellite orientation", *Journal of Geophysical Research*, Vol. 106, no. d24, pages 33,471-33,484, December 27, 2001.
- [37] Wingham, D.J.; Phalippou, L.; Mavrocordatos, C.; Wallis, D.; "The mean echo and echo cross product from a beamforming interferometric altimeter and their application to elevation measurement," *Geoscience and Remote Sensing, IEEE Transactions on* , vol.42, no.10, pp. 2305- 2323, Oct. 2004, doi: 10.1109/TGRS.2004.834352.
- [38] Wingham, DJ and Wallis, DW, "The Rough Surface Impulse Response of a Pulse-Limited Altimeter With an Elliptical Antenna Pattern". *IEEE ANTENN WIREL PR* , 9 , 232 - 235, 2010. doi:10.1109/LAWP.2010.2046471.
- [39] R. F. Voss, "Random Fractal Forgeries", in *Fundamental Algorithms for Computer Graphics*, edited by R. A. Earnshaw, pp. 805-835, Springer-Verlag, New York NY, USA,1985.

-
- [40] P. Flandrin, "On the spectrum of fractional Brownian motions", IEEE Trans. Inform. Theory., vol.35, pp. 197-199, 1989.
- [41] M.V. Berry and Z.V. Lewis, "On the Weierstrass-Mandelbrot Fractal Function", Proc. R. Soc. Lond., A, 370, pp.459-484, 1980.
- [42] A. K. Fung, *Microwave Scattering and Emission. Models and Their Applications*. Artech House, Norwood, MA, 1994.
- [43] G. Bernardi, G. Franceschetti, A. Iodice, D. Riccio, "Fractal Modeling of Altimeter Data", submitted to IEEE Transactions on Geoscience and Remote Sensing (under review).
- [44] G. Bernardi, G. Franceschetti, A. Iodice, D. Riccio, "Fractal-based modeling of altimeter data", in Proc. 2008 IEEE International Geoscience Remote Sensing Symposium Luglio 6-11, 2008, Boston, Massachusetts, U.S.A.
- [45] G. Bernardi, G. Franceschetti, A. Iodice, D. Riccio, "Un modello elettromagnetico dei dati ricevuti dal radar altimetro" in Proc. XVII RiNEm, Riunione Nazionale di Elettromagnetismo, Lecce, 15-19 Settembre 2008.
- [46] G. Bernardi, G. Franceschetti, A. Iodice, D. Riccio, "A Fractal Approach for Understanding Altimeter Data", PIERS 2010, in Xi'an, CHINA, 22-26 March, 2010.
- [47] G. Bernardi, G. Franceschetti, A. Iodice, D. Riccio, "Electromagnetic Models for a Radar Altimeter Simulator", in Proc. XVIII RiNEm, Riunione Nazionale di Elettromagnetismo, Benevento, 7-10 Settembre 2010.
- [48] G. Franceschetti, R. Lanari, *Synthetic Aperture Radar Processing*, CRC Press Inc, 1999.
- [49] "The Cassini-Huygens Mission to the Saturnian System", Dennis Matson, Space Science Reviews 104: 1-58, 2002.
- [50] JPL Publication No.D-11777, Cassini Document 699-070-2, Cassini Program Environmental Impact Statement Supporting Study.
- [51] Charles Elachi, "Cassini Titan Radar Mapper", Proceeding of the IEEE, Vol.79,N°6, June 1991

- [52] K.S. Chen, A.K. Fung, 1992, "A backscattering Model for Ocean Surface", IEEE VOL.30, N°4, 811-817
- [53] G. Alberti, L. Festa, G. Vingione, E. Flamini (Agenzia Spaziale Italiana), R. Orosei (Istituto Nazionale di Astrofisica), G. Picardi, R. Seu (Università di Roma "La Sapienza"), "The Processing of Altimetric Data (PAD) System for Cassini RADAR", VII Convegno Nazionale di Scienze Planetarie, 5-9 settembre 2006, San Felice al Circeo (LT), Italia.
- [54] G. Vingione, G. Alberti, C. Papa, L. Festa (CO.RI.S.T.A), G. Picardi, R. Seu, P.P. Del Marmo (INFO-COM, University of Rome La Sapienza), R. Orosei (IASF Istituto di Astrofisica Spaziale e Fisica Cosmica, CNR), P. Callahan, S. Wall (Jet Propulsion Laboratories, California Institute of Technology)," Processing of Altimetric Data of CASSINI mission", European Geosciences Union General Assembly 2007 Vienna, Austria, 15 - 20 aprile 2007.